COO-1195-214

A STUDY OF THE OMEGA-ZERO SPIN-DENSITY MATRIX ELEMENTS IN THE REACTION PI-MINUS PROTON GOES TO OMEGA-ZERO NEUTRON AT 3.65, 4.5, AND 5.5 GeV/c

BY

ELI IRA ROSENBERG
B.S., City College of New York, 1964
M.S., University of Illinois, 1966

THESIS

Submitted in partial fulfillment of the requirements
for the degree of Doctor of Philosophy in Physics
in the Graduate College of the
University of Illinois at Urbana-Champaign, 1971

Urbana, Illinois
June, 1971

This research was supported in part by the U.S. Atomic Energy Commission under Contract AT(11-1)-1195.

A STUDY OF THE OMEGA-ZERO SPIN-DENSITY MATRIX ELEMENTS IN THE REACTION PI-MINUS PROTON GOES TO OMEGA-ZERO NEUTRON AT 3.65, 4.5, AND 5.5 GeV/c

Eli Ira Rosenberg, Ph.D.
Department of Physics
University of Illinois at Urbana-Champaign, 1971

A study was made of the ω^o spin-density matrix elements in the reaction $\pi^- p \rightarrow \omega^o n$. The data were collected using a combination of scintillation counters and optical spark chambers designed to detect events of the type $\pi^- p \rightarrow \pi^+ \pi^- \gamma\gamma n$. Incident pions of momenta 3.65, 4.5, and 5.5 GeV/c were produced by an internal target at the Argonne National Laboratory Zero Gradient Synchrotron. The values obtained for the ω^o spin-density matrix elements are inconsistent with the predictions of a simple model which allows for Reggeized $\rho(765)$ and B(1235) exchange.

ACKNOWLEDGMENTS

I wish to express my sincere appreciation to all those who have contributed to this work.

In particular, I am deeply grateful to my advisor, Professor Hans Frauenfelder, for his guidance, encouragement, and for imparting to me a small fraction of his boundless enthusiasm for all phases of physics.

The insight and advice of Professor Albert Wattenberg was invaluable during my early contacts with experimental high-energy physics, and his continuing interest has been deeply appreciated.

I am very grateful to Professors Leland Holloway and David Mortara without whom this work would not have been possible.

My fellow graduate students Al Russell and Mick Jordan provided good fellowship and contributed much hard work to this experiment.

Among the others who have made this work possible are: the tireless Dr. Bent Huld; Professors Don McLeod, Sy Margulies, and Seymour Bernstein of the Chicago Circle Campus; Dr. Martin Garrell; our technicians Cloyd Smock and Leonard Seward; the ZGS staff, and the Argonne AMD staff.

The author is also grateful to Professor James H. Smith, Bob Cullum, and David Eitelbach for their amazing job of programming and maintaining the $\Sigma 2$ computer.

I also wish to thank:

the U.S. Atomic Energy Commission for their financial support, of this experiment,

Mrs. Sherry Kallembach for typing this manuscript,

Mrs. Mary Jo Pelafas and her scanning and measuring crew,

Mrs. Nancy Czechowski and the staff of the 7094, and Mrs. Estelle Thomas.

I wish to thank my parents who gently instilled the love of knowledge and science which made this work possible.

Finally, I express my most profound gratitude to Eileen and Elliot who made hard sacrifices on the basis of love and trust, and without whom all this would be insignificant.

TABLE OF CONTENTS

I. INTRODUCTION

An investigation of the reaction

$$\begin{array}{l}\pi^- p \to \omega^o n \\ \quad\ \llcorner\!\!\longrightarrow \pi^+ \pi^- \pi^o\end{array} \qquad (I.1)$$

was carried out at the Argonne National Laboratory Zero Gradient Synchrotron using optical spark chambers and scintillation counters. The purpose of this experiment was to obtain the differential cross section, $d\sigma/dt$, and the experimentally accessible ω^o spin density matrix elements over a significant range of momentum transfer $.04 \le |t| < 1.0$ GeV^2/c^2 for several incident beam momenta (3.65, 4.5, and 5.5 GeV/c).

The reaction I.1 has several properties which render it amenable to theoretical analysis. In any peripheral model (we have in mind a simple Regge model), conservation of isospin and G-parity restrict the nature of the exchange system. In particular, at the $\pi^+\omega^o$ vertex in the t-channel, $I^G = 1^+$. Of the known, low-lying mesons only the ρ($J^P = 1^-$, M = 765 MeV/c^2), a vector meson, and the B ($J^P = 1^+$, M = 1235 MeV/c^2), an axial-vector meson have $I^G = 1^+$, and thus are candidates for the exchange mechanism.[3]

If we work in the t-channel helicity frame (the coordinate system of Gottfried and Jackson), parity conservation imposes restrictions on the exchange amplitudes which are easily expressed in terms of the ω^o spin density matrix elements and can be used to establish the existence of some unnatural parity exchange, i.e., B exchange. G-parity conservation in this coordinate system also imposes restrictions on the B contribution.

Reaction I.1 is well-suited to optical spark chamber and counter techniques rather than to low-density liquid bubble chambers. The presence of the multi-neutral particle final-state (the neutron and the $\pi^0 \to \gamma\gamma$) forces the bubble chamber experiments to look at the charge symmetric reaction ($\pi^+ n \to \omega^0 p$) in the form[25,26,27]

$$\pi^+ d \to \omega^0 n(p_s) \qquad (I.2)$$

These experiments are limited statistically by the non-triggerability of most bubble chambers, and involve the problems of clearly identifying the spectator protons and of renormalizing the extremely low $|t|$ region because of the Pauli exclusion principle.

This report describes the measurement of the ω^0 spin density matrix elements. Chapter II gives some theoretical background as to what one might expect to see. Chapter III describes the experimental technique with regard to data collection. Chapter IV describes the data reduction and analysis. Chapter V gives the results and conclusions. The Appendix expands on several items only briefly mentioned in the main text.

We find that the predictions of a simple model combining ρ- and B-exchange are not consistent with the data.

II. THEORETICAL BACKGROUND

A. Properties of the ω^o and Its Spin Density Matrix

The existence of a tripion isosinglet resonance of mass near 785 MeV/c^2 was established in 1961 by Maglic et al.[1] in the reaction

$$\bar{p}p \rightarrow \pi^+\pi^-\pi^o\pi^+\pi^-$$

Subsequent analyses of tripion Dalitz plots established the spin and parity of the ω^o to be $J^P = 1^-$.[2] The currently accepted values of the mass and width are 783.7 MeV/c^2 and 11.9 MeV/c^2 respectively.[3]

The spin density matrix takes the form

$$\tilde{\rho} = \begin{pmatrix} \rho_{11} & \rho_{10} & \rho_{1-1} \\ \rho_{10}^* & \rho_{00} & -\rho_{10}^* \\ \rho_{1-1} & -\rho_{10} & \rho_{11} \end{pmatrix} \quad \text{with } \rho_{00} = 1-2\rho_{11};\ \rho_{11}, \rho_{1-1} \text{ real} \qquad \text{(II.1)}$$

for a spin one object, produced in a two body interaction, in its rest frame, with z the quantization axis, the y axis normal to the production plane, and the x axis chosen to make a right-handed coordinate system. We have assumed parity conservation in the production mechanism and thus need four independent real quantities to determine $\tilde{\rho}$; ρ_{11}, ρ_{1-1}, Re ρ_{10}, and Im ρ_{10}.

In the rest frame of the resonance, the matrix element describing the decay of an $I^G = 1^-$, $J^P = 1^-$ object into three pions (note $\omega^o \rightarrow 3\pi^o$ is not allowed) can be written[4]

$$m \sim \vec{\epsilon}\cdot\vec{n} \; ; \qquad \vec{n} = \vec{p}_{\pi^+} \times \vec{p}_{\pi^-} = -\vec{p}_{\pi^+} \times \vec{p}_{\pi^o} = \vec{p}_{\pi^-} \times \vec{p}_{\pi^o} \qquad \text{(II.2)}$$

where $\vec{\epsilon}$ is the polarization vector of the decaying vector meson, and $\vec{n}$ is the normal to the decay plane. The normal's angular distribution ($W \sim |m|^2$) is then easily found.

If one chooses a coordinate system as described in the paragraph preceeding equation (II.1),

$$W(\theta,\varphi) = \frac{3}{4\pi}[\rho_{oo}\cos^2\theta + \rho_{11}\sin^2\theta - \rho_{1-1}\sin^2\theta\cos 2\varphi - \sqrt{2}\,\mathrm{Re}\,\rho_{10}\sin 2\theta\cos\varphi]$$

$$\text{where} \quad \vec{n}\to\hat{n} = (\sin\theta\cos\varphi,\ \sin\theta\sin\varphi,\ \cos\theta) \qquad \text{(II.3)}$$

with θ,φ the usual polar and azimuthal angles. (See Appendix B.) The factor of $3/4\pi$ normalizes $W(\theta,\varphi)$ i.e., $\int W(\theta,\varphi)d\cos\theta\, d\varphi = 1$. Only Im ρ_{10} cannot be determined without the use of a polarized target. However, further restrictions on the density matrix elements do exist independent of the production process.

In particular, since the eigenvalues of $\tilde{\rho}$ must be positive, i.e., $\lambda_i \geq 0$ $(i = 1,2,3)$ we find as strict mathematical consequences:[5,6]

$$\sum \lambda_i = \mathrm{Tr}\tilde{\rho} \geq 0 \qquad \text{(II.4a)}$$

$$\lambda_1\lambda_2 + \lambda_2\lambda_3 + \lambda_3\lambda_1 = \frac{1}{2}[(\mathrm{Tr}\tilde{\rho})^2 - \mathrm{Tr}\tilde{\rho}^2] \geq 0 \qquad \text{(II.4b)}$$

$$\lambda_1\lambda_2\lambda_3 = \frac{1}{6}[2\mathrm{Tr}\tilde{\rho}^3 + (\mathrm{Tr}\tilde{\rho})^3 - 3\mathrm{Tr}\tilde{\rho}\mathrm{Tr}\tilde{\rho}^2] \geq 0 \qquad \text{(II.4c)}$$

II.4a is trivially satisfied since $\mathrm{Tr}\tilde{\rho} = 1$ by conservation of probability. II.4b reduces to $\mathrm{Tr}\tilde{\rho}^2 \leq 1$ which is also well known, where the equality holds for $\lambda_j = 1$, $\lambda_{i\neq j} = 0$, i.e., pure states.

II.4c reduces to $2\mathrm{Tr}\tilde{\rho}^3 - 3\mathrm{Tr}\tilde{\rho}^2 + 1 \geq 0$.

If we combine II.4b and II.4c and work in the coordinate system used above we find

$$\rho_{1-1} \leq \rho_{11} \tag{II.5a}$$

$$2(\mathrm{Re}\rho_{10})^2 \leq 2|\rho_{10}|^2 \leq \rho_{00}(\rho_{11}-\rho_{1-1}) \tag{II.5b}$$

B. General Properties of the ω^o Production

In this section, we work in the t-channel helicity frame, and consider amplitudes which describe the t-channel process

$$p\bar{n} \to \pi^+\omega^o \tag{II.6}$$

for physical t. The extension of the relationships derived below to the physical s-channel, i.e., for the reaction

$$\pi^- p \to \omega^o n$$

is guaranteed if the analytic continuation of the appropriate functions, i.e., t-channel amplitudes or various algebraic functions of the t-channel amplitudes, is unique. The uniqueness of the analytic continuation can be shown to hold by using Carlson's theorem plus the assumption that the

Mandelstam representation is valid with only a finite number of subtractions.[7] By not specifying the analytic continuation, we shall derive results which have general validity, i.e., are independent of Regge asymptotics.

The partial wave expansion of a t-channel helicity amplitude describing the t-channel reaction AB→CD is given by

$$f_{CD;AB} = \sum_J (2J+1)\, F^J_{CD;AB}\, d^J_{\lambda\mu}(\theta) \tag{II.7}$$

where θ is the t-channel center-of-momentum scattering angle; $F^J_{CD;AB}$ is the matrix element connecting two Jacob-Wick helicity states of spin J; A, B, C, and D are the helicities of the respective particles; $\lambda = A-B$, $\mu = C-D$; and $d^J_{\lambda\mu}(\theta)$ is the Wigner rotation function. (Our notation, conventions, and relation to the notation of Jacob and Wick, are described in Appendix A)

Defining helicity states of definite parity, we find the matrix element between two such states (for baryon number zero states) to be given by

$$F^{J\eta}_{CD;AB} = \frac{1}{2}\left(F^J_{CD;AB} + \eta\eta_C\eta_D(-1)^{S_C+S_D} F^J_{-C-D;AB}\right) \tag{II.8}$$

where η_C, η_D are the intrinsic parities of particles C and D; S_C and S_D are their spins; and the intrinsic parity of an intermediate state of spin J is given by $\eta(-1)^J$. $\eta = 1$ for natural parity; $\eta = -1$ for unnatural parity.

Thus we have

$$F^{J\eta}_{-C-D;AB} = \eta\eta_C\eta_D(-1)^{S_C+S_D}\, F^{J\eta}_{CD;AB} \tag{II.9a}$$

Similarly

$$F^{J\eta}_{CD;-A-B} = \eta\eta_A\eta_B(-1)^{S_A+S_B} F^{J\eta}_{CD,AB} \tag{II.9b}$$

(All relations involving helicity flips of A and B, rather than C, D can be derived using equation A.11 of Appendix A.) In our case

$$\eta_C\eta_D(-1)^{S_C+S_D} = \eta_\pi\eta_\omega(-1)^{S_\pi+S_\omega} = -1 \tag{II.9a'}$$

$$\eta_A\eta_B(-1)^{S_A+S_B} = \eta_p\eta_{\bar{n}}(-1)^{S_p+S_{\bar{n}}} = +1 \tag{II.9b'}$$

Let us define

$$f^{\eta}_{CD;AB} = \sum_J (2J+1)\, F^{J\eta}_{CD;AB}\, d^J_{\lambda\mu}(\theta) \tag{II.10}$$

Because of the symmetry properties of the d-functions, the $f^{\eta}_{CD,AB}$ do not, in general, satisfy a simple symmetry property analogous to equations II.9a and II.9b. However, if $\lambda=0$, i.e., A=B

$$d^J_{o-\mu}(\theta) = \left[\frac{(J-\mu)!}{(J+\mu)!}\right]^{1/2} P^{\mu}_J(\theta) \;; \qquad \mu \geq 0 \tag{II.11}$$

where $P^{\mu}_J(\theta)$ is an associated Legendre polynomial. From the property of the P^{μ}_J under $\theta\to\pi+\theta$

$$P_J^{\mu}(\pi+\theta) = (-1)^J P_J^{\mu}(\theta)$$

we find

$$d^J_{o-\mu}(\theta) = (-1)^{\mu} d^J_{o\mu}(\theta) \qquad \text{(II.12)}$$

Thus

$$f^{\eta}_{-C-D;AB} = \eta\eta_C\eta_D(-1)^{\mu+S_C+S_D} f^{\eta}_{CD;AB} \qquad \text{for } \lambda=0=A-B$$

Using II.9a', we have

$$f^{\eta}_{-C-D;AA} = -\eta(-1)^{\mu} f^{\eta}_{CD;AA} \qquad \text{(II.13a)}$$

Using similar arguments for the case $\mu=0$, we find

$$f^{\eta}_{CD;AB} = \eta\eta_A\eta_B(-1)^{S_A+S_B+\lambda} f^{\eta}_{CD;-A-B}$$

$$= \eta\eta_C\eta_D(-1)^{S_C+S_D} f^{\eta}_{-C-D;AB}$$

or

$$f^{\eta}_{CC;AB} = -\eta f^{\eta}_{-C-C;AB} \qquad \text{(II.13b)}$$

We make the change in notation $A=\lambda_{\bar{n}}$, $B=\lambda_p$, $C=\lambda_{\pi}$, $D=\lambda_{\omega}$ and add $\lambda_{\pi}\equiv 0$, so that II.13a and II.13b become

$$f^{\eta}_{o-\lambda_{\omega};\lambda_{\bar{n}}\lambda_p=\lambda_{\bar{n}}} = -\eta(-1)^{\lambda_{\omega}} f^{\eta}_{o\lambda_{\omega};\lambda_{\bar{n}}\lambda_p=\lambda_{\bar{n}}} \qquad \text{(II.13a')}$$

$$f^{\eta}_{oo;\lambda_{\bar{n}}\lambda_p} = -\eta f^{\eta}_{oo;\lambda_{\bar{n}}\lambda_p} \qquad \text{(II.13b')}$$

Before drawing conclusions from equation II.13a' and II.13b', we will derive the condition under which $\lambda=A-B=\lambda_{\bar{n}}-\lambda_p=0$, i.e., under which II.13a' holds.

Consider a nucleon-antinucleon vertex, such as the $p\bar{n}$ vertex for reaction II.6. G-parity for the $N\bar{N}$ system is given by

$$G = (-1)^{L+S+I}$$

where S is the total $N\bar{N}$ spin, L is their relative angular momentum, and I is the total isospin. If an intermediate state has parity $P = \eta\tau$ where $\tau = (-1)^J$ is the signature of a Regge trajectory containing this state, then parity conservation yields

$$\eta\tau = -(-1)^L$$

Conservation of isospin and G-parity, then gives

$$(-1)^S = -\eta\tau G(-1)^I$$

Setting S=0, requires $\lambda_N = \lambda_{\bar{N}}$, thus II.13a' will hold if

$$-1 = \eta\tau G(-1)^I \qquad \text{(II.14)}$$

For the two possible exchange systems ρ and B

$$\eta_\rho \tau_\rho G_\rho(-1)^{I_\rho} = +1$$

and

$$\eta_B \tau_B G_B (-1)^{I_B} = -1$$

Thus II.13a' holds for B exchange.

Since $\eta_B = -1$, $\eta_\rho = +1$, we find from II.13a', for B exchange

$$f^{-}_{o-1;\lambda_{\bar{n}}\lambda_p=\lambda_{\bar{n}}} = -f^{-}_{o1;\lambda_{\bar{n}}\lambda_p=\lambda_{\bar{n}}} \tag{II.15}$$

and from II.13b', for ρ exchange

$$f^{+}_{oo;\lambda_{\bar{n}}\lambda_p} = -f^{+}_{oo;\lambda_{\bar{n}}\lambda_p} = 0 \tag{II.16}$$

Equation II.16 expresses the fact that ρ exchange cannot couple to $\lambda_\omega=0$. This result can also be derived by considering parity conservation at the πω vertex alone.[8,9]

The ω^o spin-density matrix in the Gottfried-Jackson frame is given by[8]

$$\rho_{\lambda\lambda'} = \sum_{ABC} f_{c\lambda;AB} \, f^{*}_{c\lambda';AB} \tag{II.17}$$

For pure B-exchange

$$\rho_{\lambda\lambda'} = \sum_{A} f^{-}_{o\lambda;AA} \, f^{-*}_{o\lambda';AA} = 2(f^{-}_{o\lambda;++} \, f^{-*}_{o\lambda';++})$$

and we find

$$\rho_{11} = -\rho_{1-1} \qquad \text{(pure B-exchange)} \tag{II.18}$$

and

$$|\rho_{10}|^2 = \rho_{oo}\rho_{11} \qquad \text{(pure B-exchange)} \qquad \text{(II.19)}$$

For pure ρ-exchange

$$\rho_{oo} = \rho_{10} = 0 \qquad \text{(pure } \rho\text{-exchange)} \qquad \text{(II.20)}$$

Finally, we consider the possibility of both ρ and B exchange, so

$$\rho_{\lambda\lambda'} = \sum_{AB} \left(f^{+}_{o\lambda;AB} + f^{-}_{o\lambda;AB}\right)\left(f^{+}_{o\lambda';AB} + f^{-}_{o\lambda';AB}\right)^{*}$$

$$= \rho^{+}_{\lambda\lambda'} + \rho^{-}_{\lambda\lambda'} + \rho^{\mathrm{Int}}_{\lambda\lambda'}$$

where $\rho^{\pm}_{\lambda\lambda'} = \Sigma_{AB}\, f^{\pm}_{o\lambda;AB}\, f^{\pm *}_{o\lambda';AB}$ represent the contribution from pure ρ- and B-exchange respectively, and where

$\rho^{\mathrm{Int}}_{\lambda\lambda'} = \Sigma_{AB}\,(f^{+}_{o\lambda;AB}\, f^{-*}_{o\lambda';AB} + f^{-}_{o\lambda;AB}\, f^{+*}_{o\lambda';AB})$ represents the contribution from interference terms.

Since $f^{-}_{o\lambda;AB} = 0$ for $A \neq B$, we have

$$\rho^{\mathrm{Int}}_{\lambda\lambda'} = f^{+}_{o\lambda++}\, f^{-*}_{o\lambda'++} + f^{-}_{o\lambda++}\, f^{+*}_{o\lambda'++} + f^{+}_{o\lambda--}\, f^{-*}_{o\lambda'--} + f^{-}_{o\lambda--}\, f^{+*}_{o\lambda'--}$$

From II.13a and A.11

$$f^{\eta}_{o\lambda_\omega;\lambda_{\bar n}\lambda_p=\lambda_{\bar n}} = \eta\, f^{\eta}_{o\lambda_\omega;-\lambda_{\bar n}-\lambda_p=-\lambda_{\bar n}}$$

Thus

$$\rho_{\lambda\lambda'}^{Int} = 0, \text{ and } \rho_{\lambda\lambda'} = \rho_{\lambda\lambda'}^{+} + \rho_{\lambda\lambda'}^{-}.$$

In summary, we have

1) Pure ρ-exchange:

$$\rho_{oo} = \rho_{10} = 0 \qquad \text{(II.20)}$$

2) Pure B-exchange:

$$\rho_{11} = -\rho_{1-1} \qquad \text{(II.18)}$$

$$|\rho_{10}|^2 = \rho_{11}\rho_{oo} = \frac{1}{2}\,\rho_{oo}(\rho_{11}-\rho_{1-1}) \qquad \text{(II.19)}$$

3) ρ- and B-exchange:

$$\rho_{oo} = \rho_{oo}^{-} \qquad \text{(II.21a)}$$

$$\rho_{10} = \rho_{10}^{-} \qquad \text{(II.21b)}$$

$$\rho_{1-1} = \rho_{1-1}^{+} + \rho_{1-1}^{-} = \rho_{1-1}^{+} - \rho_{11}^{-} \qquad \text{(II.21c)}$$

$$\rho_{11} = \rho_{11}^{+} + \rho_{11}^{-} \qquad \text{(II.21d)}$$

$$\rho_{11} + \rho_{1-1} = \rho_{11}^{+} + \rho_{1-1}^{+} \qquad \text{(II.22)}$$

The important results are II.21a and II.22 which give an immediate check on the presence of any B-exchange and any ρ-exchange.

C. Predictions of Simple Regge Models

The procedure to be used in Reggeizing the t-channel helicity amplitudes given in equation II.7 has been discussed by many authors.[10,11,12] We restrict ourselves to the exchange of simple Regge trajectories. Since we are dealing with particles of unequal mass having spin, care must be taken near the forward direction, i.e., as $s\to\infty$, $\cos\theta_t\to\infty$ except near

$|t| = |t|_{min}$. In this low $|t|$ region, the d-functions fail to satisfy a simple symmetry property under $\lambda \to -\lambda$ or $\mu \to -\mu$. However, for $\cos\theta_t \to \infty$, i.e., outside of this low $|t|$ region, we find

$$d^J_{\lambda -\mu}(\theta) = (-1)^\mu d^J_{\lambda\mu}(\theta) \qquad \text{for all } \lambda \text{ and } \mu$$

Thus as a consequence of letting $s \to \infty$ during Reggeization, we find, except for the region $|t| \approx |t|_{min}$,[13]

$$f^\eta_{-C-D;AB} = -\eta(-1)^\mu f^\eta_{CD;AB} \tag{II.23}$$

In terms of density matrix elements, we have for all natural parity exchange, such as ρ exchange

$$\rho_{oo} = \rho_{10} = 0 \tag{II.24a}$$

$$\rho_{11} = \rho_{1-1} \tag{II.24b}$$

and for all unnatural parity exchanges, such as B exchange

$$\rho_{11} = -\rho_{1-1} \tag{II.24c}$$

$$|\rho_{10}|^2 = \rho_{oo}\rho_{11} = \frac{1}{2}\rho_{oo}(\rho_{11} - \rho_{1-1}) \tag{II.24d}$$

All of these results, except II.24b were previously obtained in section II.B for ρ and B exchange independent of Regge asymptotics. From equation II.23

it can be shown that there are no interference terms between the natural and unnatural parity exchanges.

If only one unnatural parity trajectory is exchanged, then

$$\text{Im}\ \rho_{10} = 0 \qquad \text{(II.25)}$$

since the Regge assumption implies all amplitudes of the same trajectory to have equal phases. If more than one unnatural parity trajectory is exchanged, equation II.25 will hold only if all these trajectories have the same phase.

For a model which allows only a combination of Regge trajectory exchanges, we can conclude as $s\to\infty$ and $\cos\theta_t\to\infty$, ρ_{00} and $\rho_{11}-\rho_{1-1}$ only have contributions from unnatural parity exchange; $\rho_{11}+\rho_{1-1}$ only has contributions from natural parity exchange.[13]

For a model which allows only Reggeized ρ and B exchanges, we can conlcude as $s\to\infty$ and $\cos\theta_t\to\infty$, $\text{Im}\ \rho_{10} = 0$; ρ_{oo} and $\rho_{11}-\rho_{1-1}$ only have contributions from B exchange; $\rho_{11}+\rho_{1-1}$ only has contributions from ρ exchange.

Several authors have described models using ρ and/or B exchange.[14-16] The parameters of the ρ trajectory are well known and lead to a nonsense-wrong-signature zero at $t \approx -.6(\text{GeV}/c)^2$. Incorporating this into our model, we predict at $t \approx -.6(\text{GeV}/c)^2$ and as $s\to\infty$, $\cos\theta_t\to\infty$

$$(\text{Re}\rho_{10})^2 = \rho_{10}^2 = \rho_{oo}\rho_{11} = \frac{1}{2}\rho_{oo}(\rho_{11}-\rho_{1-1})$$

$$\rho_{11} + \rho_{1-1} = 0$$

Finally we note that since ρ_{00} only has contributions from B exchange, the effects of ρ-ω interference may be more transparent in ρ_{00}. In order to reach this conclusion, we must assume that the effects of ρ-ω interference manifest themselves in the ω^0 production amplitude for reaction I.1, and that this interference occurs between production amplitudes having the same spin structure under isospin violation.[17] Since at low $|t|$ the ρ production amplitude is dominated by π- exchange, we expect the interference to take place in the B-exchange amplitudes for ω^0 production at low $|t|$. (We note that at least one set of authors have concluded that the ρ and B trajectories are exchange degenerate.[18]) There will then be a difference at low $|t|$ between ρ_{00} for $\pi^+ n \rightarrow \omega^0 p$ and ρ_{00} for $\pi^- p \rightarrow \omega^0 n$.

III. EXPERIMENTAL TECHNIQUE 1: DATA COLLECTION

The data was collected using a combination of scintillation counters and optical spark chambers. This apparatus was designed and arranged to detect events corresponding to reaction I.1 in the momentum transfer range $.04 \le |t| \le 1.0\ (\mathrm{GeV/c})^2$. The source of pions was the beam described below, and the source of protons was a liquid Hydrogen target.

The scintillation counters can be grouped into four categories: (1) a beam defining telescope, (2) a neutron counter hodoscope, which measured the outgoing neutron's position and time-of-flight, (3) a set of anti-counters, which were used to veto out interactions producing charged particles at angles incompatible with reaction I.1 kinematics for neutrons in our neutron hodoscope, and (4) a π counter hodoscope, which was used to require two outgoing charged particles in the forward direction.

The optical spark chambers were used to convert the π^o decay photons and to provide for identification of and positional measurement of the charged pion tracks.

A. The Beam

The experiment was performed at the Argonne Zero Gradient Synchrotron Beam No. 17, an unseparated π^- beam produced by circulating protons targeting internally on a target which also serves to extract protons for the first external proton beam. The secondary particles are directed down the 17° beam line by a transport system consisting of three quadrupole doublets and two bending magnets shown in figure III-1. A freon gas Čerenkov counter located in the beam was used as a threshold counter

Figure III-1. Beam transport system. The neutron counters are visible in the upper right-hand corner.

BEAM TRANSPORT SYSTEM
ARGONNE ZGS EXPERIMENT E-201

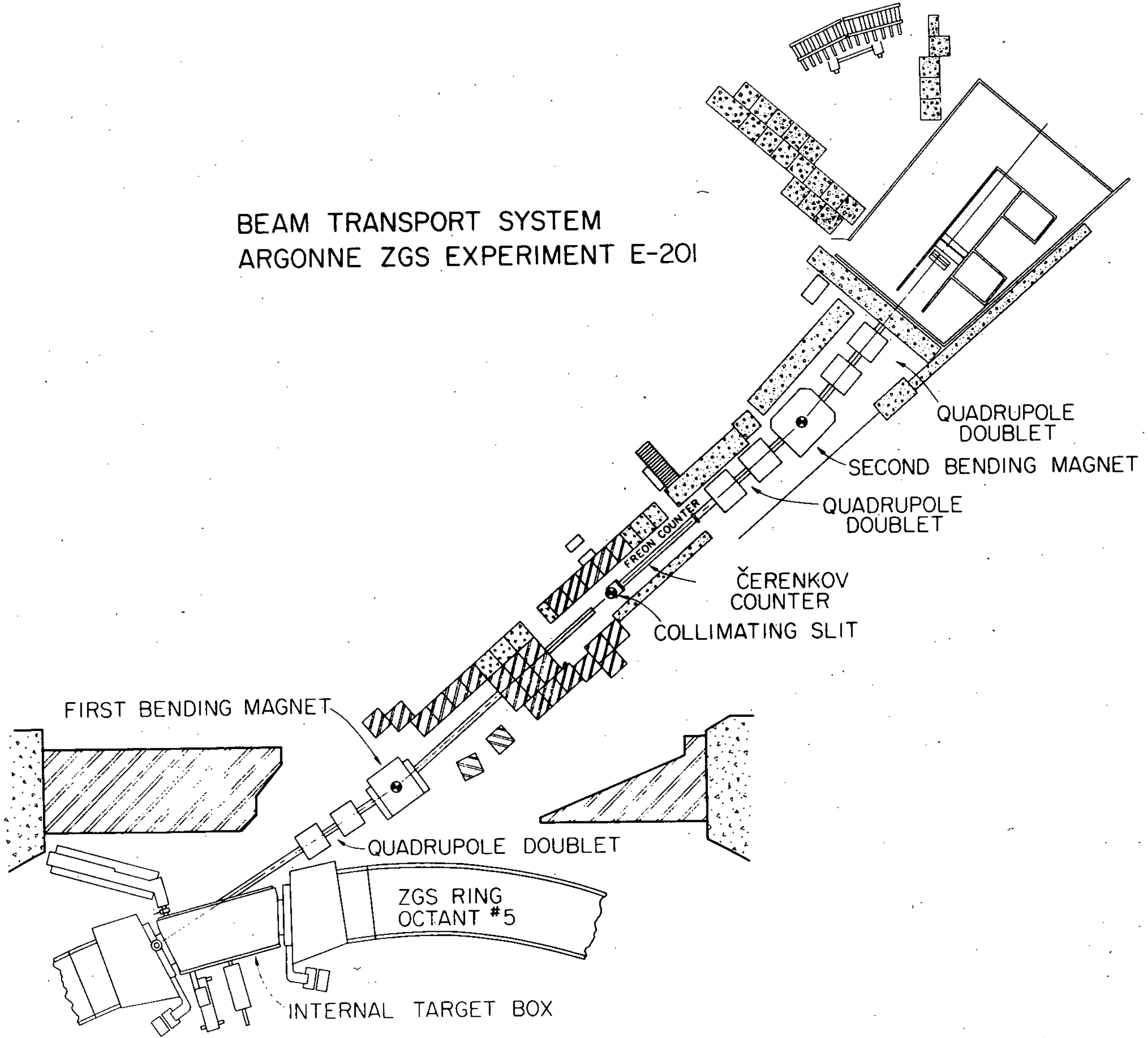

in vetoing electrons and muons. Just upstream of this counter is an adjustable collimating slit which was used to regulate the beam intensity. At the widest opening of this slit, the beam momemtum bite was $|\frac{\Delta p}{p}| \leq 1\%$, and for most of the data $|\frac{\Delta p}{p}| \leq .75\%$.

The transport system was adjusted to pass particles of either 3.65, 4.5, or 5.5 GeV/c momentum. The intensity was held between 100,000 and 200,000 beam particles per ZGS pulse in our beam telescope. The pulses were of 450-600 milliseconds duration, occurring approximately once every 3 seconds.

The final focus occurred between scintillation counters B2 and HA (see figure III-2), and resulted in a spot size at the upstream end of our liquid Hydrogen target of 32mm horizontal×13mm vertical with a horizontal half-angle divergence of 4 milliradians and a vertical half-angle divergence of 7 milliradians.

B. Experimental Layout

The experimental layout is shown in figure III-2. Counters B_o, B_1, and B_2 provide a beam telescope. The 5cm diameter x 30cm liquid hydrogen target was surrounded on five sides by a set of anti-counters, SA_1 -SA_5 and HA, with the upstream counter, HA, having a 19mm diameter hole allowing for the passage of the beam. Additional anti-counters WA_1 -WA_5 (not shown in the figures) were arranged to veto out charged particles emerging from the target in the forward direction but at angles too large to be consistent with ω^o production and subsequent decay.

The target was designed and constructed by the Argonne Liquid Hydrogen Target Group, and was of the closed system type. This target

Figure III-2 Experimental Layout.

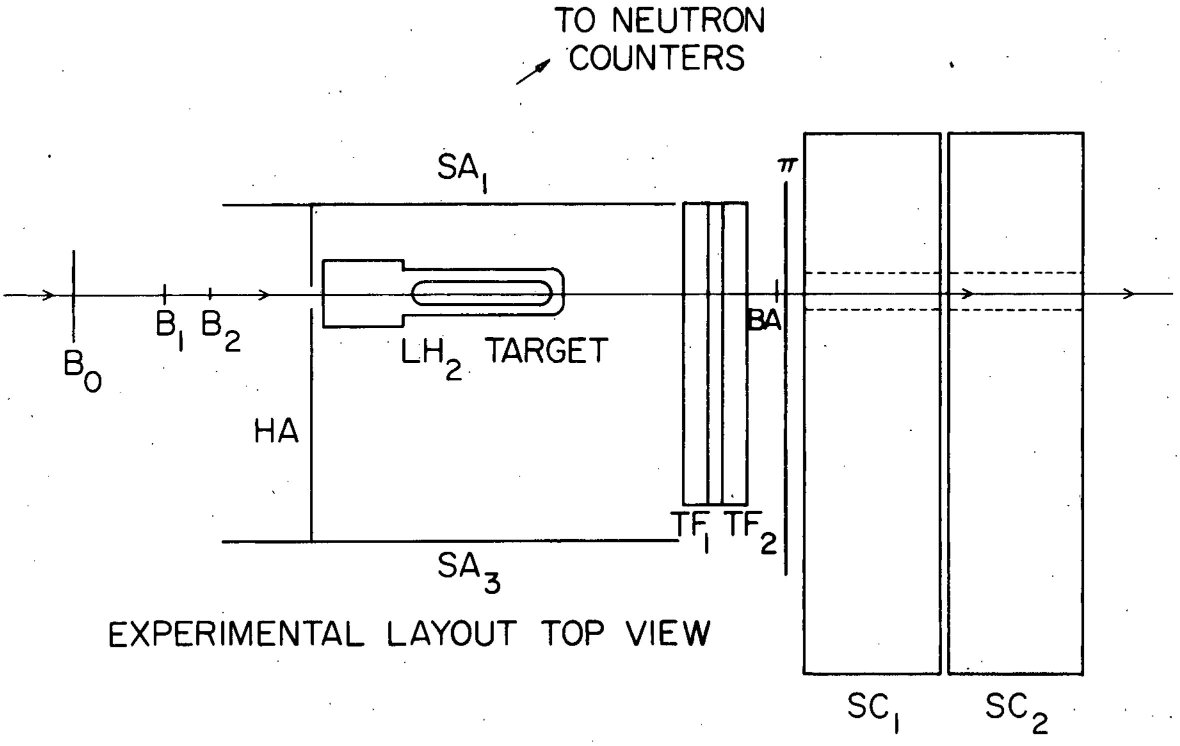

EXPERIMENTAL LAYOUT TOP VIEW

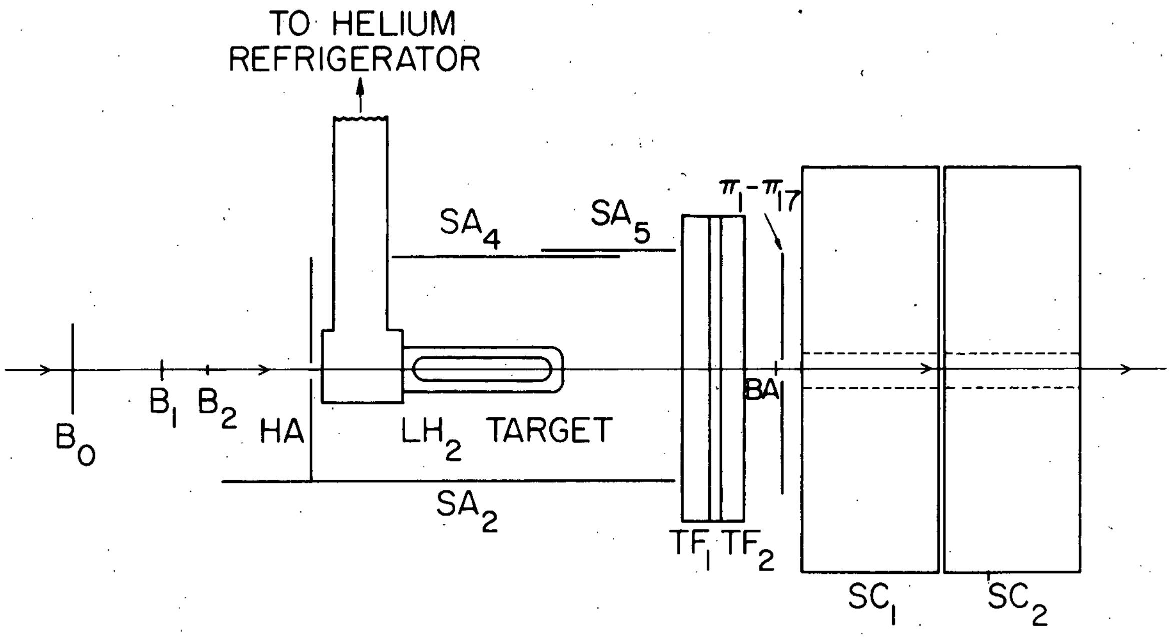

EXPERIMENTAL LAYOUT SIDE VIEW

system used a 10-watt helium refrigeration unit which was mounted above the target as indicated in the figure.

The two spark chambers TF_1 and TF_2, used thin Aluminum foil plates of fiducial area 69cm x 69cm and consisted of a total of eight 1cm gaps for identification of the charged pions. Counter BA was a beam-anti counter, and counters π_1-π_{17} formed a horizontal hodoscope which was used to detect the two charged pions. (Table III.1 gives details on all the scintillation counters.) Two 91cm x 122cm shower chambers SC_1 and SC_2, allowed visual identification of the π^o produced photons. SC_1 had 21 3.2mm plates; the first seven plates were of Aluminum and these seven gaps helped in identifying the charged pions. The remaining 14 plates in SC_1 and all 21 plates in SC_2 consisted of .76mm Al - 1.52mm Pb-.76mm Al sandwiches. The gap width in both of the shower chambers was 1cm. The two shower chambers represented ~9.5 radiation lengths of material for conversion of the photons. A 76mm diameter hole through the center of the shower chambers allowed for passage of the beam particles.

The chambers were photographed in 90° stereo using a 150mm focal length lens at f/11 and a Flight Research Model 207 camera. Both the top and side views of the chambers appeared on a double 35mm frame of Eastman Kodak RAR 2479 film. The camera was located immediately downstream from and slightly above the spark chambers; the chamber images were optically transported by a system of front aluminized mirrors.

A 52 element neutron-counter hodoscope was located at a distance of 10m from the target, as shown in figure III-1. The counters were arranged in a 13 (horizontal) x 4 (vertical) with a horizontal spacing of

Table III.1 Scintillation Counter Specifications

Counter	Type of Scintillator	Size (HxVxD)† units are cm	Photomultiplier Type	Comments
B_o	Pilot B	20x20x.63	RCA 8575	Extra power supplies connected to last 4-Dynodes to Prevent Voltage "sag".
B_1	" "	3.8x3.8x.32	RCA 8575	
B_2	" "	.19 diam x .16	RCA 8575	
BA	" "	3.17x3.8x.32	RCA 8575	
HA	Pilot Y	76x50.8x.95	Amperex 58AVP	Off Center 3/4" diam. for passage of beam
SA_1	" "	.95x50.8x100.2	Amperex 58AVP	
SA_2	" "	76x.95x100.2	Amperex 58AVP	
SA_3	" "	.95x50.8x100.2	Amperex 58AVP	
SA_4	" "	78.5x.95x50.8	Amperex 58AVP	
SA_5	" "	81x.95x30.5	RCA 6810A	
WA_1	" "	20x91x.95	RCA 6810A	
WA_2	" "	20x91x.95	RCA 6810A	
WA_3	" "	20x122x.95	RCA 6810A	
WA_4	" "	20x122x.95	RCA 6810A	
WA_5	Pilot B	20x61x.95	RCA 6810A	
π_1-π_8, π_{10}-π_{17}	Pilot B	91x3.17x1.77	RCA 6199	
π_9	" "	67x3.17x1.77	RCA 6199	
Neutron Counters	NE 102	10x25.4x30.5††	Amperex 58AVP	Zener Diode Base for better voltage Regulation

†Horizontal x vertical x depth presented to a beam particle

††D is depth presented to nromally incident neutron

Figure III-3 Neutron Counters as Seen by Target.

NEUTRON COUNTERS AS SEEN FROM TARGET

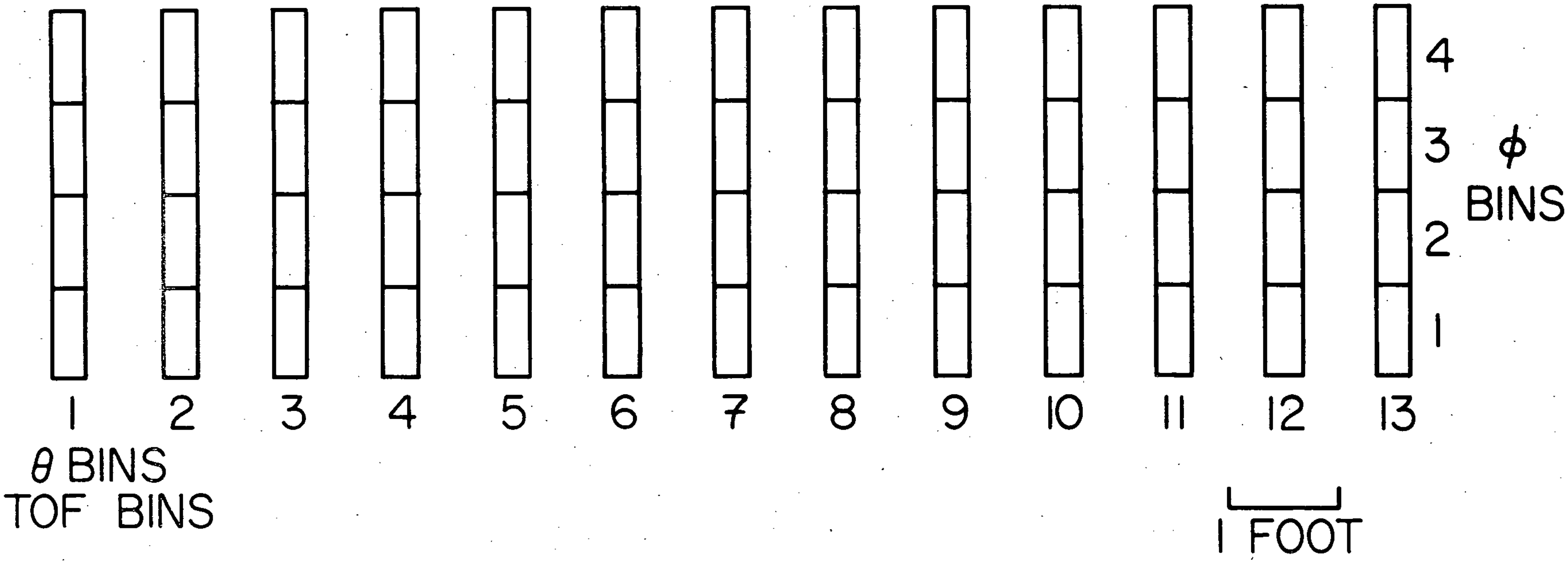

approximately twice a counter width, as illustrated in figure III-3. At each of the incident beam momenta, a central location for these counters was defined so as to insure the momentum transfer was in the range $.04 \leq |t| \leq 1.0$ (GeV/c)^2. During each series of three runs, the neutron counters were kept at central position for the first run, and then moved a counter width to alternate sides of this central position on each of the next two runs so as to make the momentum transfer acceptance continuous. In addition, these counters were rotated about a central pivot point at each beam momentum so that the arc they were laid along faced the center of the target.

The target position was changed at each of the incident beam momenta in order to assure maximum utilization of the fiducial volumes of the spark chambers.

C. Electronic Logic

The electronic logic consisted of a combination of University of Illinois, EGG, and LeCroy fast logic modules. The neutron counter logic (see figure III-5) required four output signals from each neutron counter. Anode and dynode signals from each counter in a vertical column of four were separately passively added to produce 13 "θ" signals (inverted from the last dynode output) and 13 "tof" signals (from the anode). The other anode output (each phototube base on the neutron counters produced two 50Ω anode output signals) were added passively thirteenfold; each horizontal row of 13 counters producing an individual signal. The 13th dynode signals were passively added for all 52 neutron counters and provided pulse height information.

The main logic is diagrammed in figures III-4 and III-5. An "event" "triggering" our spark chambers consisted of

$$\overline{\check{C}}\ \overline{HA}\ \overline{SA}_{1-5}\ \overline{WA}_{1-5}\ \overline{BA}\ (B_oB_1B_2)'\ (2\pi)\ \theta$$

i.e., no signal from any of the anti-counters or the Čerenkov counter; a coincidence in the beam telescope counters, but no beam particle occurring within a time interval either 130 nsec before or after the beam particle under consideration;* two and only two elements of the π hodoscope firing; and a neutron counter "θ" occurring within a predetermined time gate for a given neutron counter. Such an "event" fired the spark chambers and associated fiducials, advanced the camera, enabled an EGG time-to-amplitude converter (TAC) which recorded the interval between the firing of counter B_1 and the neutron "tof" signal, and placed indicative information on: (1) a set of binary indicators which were photographed with the spark chambers, and (2) a LeCroy data bus. The information recorded on film through the use of neon-light binary indicators was run number, "event" (frame) number, neutron time-of-flight (the TAC output converted by a LeCroy 8 bit ADC), neutron pulse height as recorded in a 8 bit LeCroy ADC, neutron θ number and neutron φ number.

The LeCroy data bus sent the information on the binary lights and the numbers of the two elements of the π hodoscope firing to the University of Illinois XDS Σ2 computer. (A Kennedy incremental tape

---

*The 130 nsec corresponded to the maximum time allowed for a stop signal from the neutron counters. The necessary logic was achieved through the use of an EGG pile-up gate module.

Figure III-4 Main Logic Diagram.

TRIGGER AND TIME OF FLIGHT LOGIC DIAGRAM

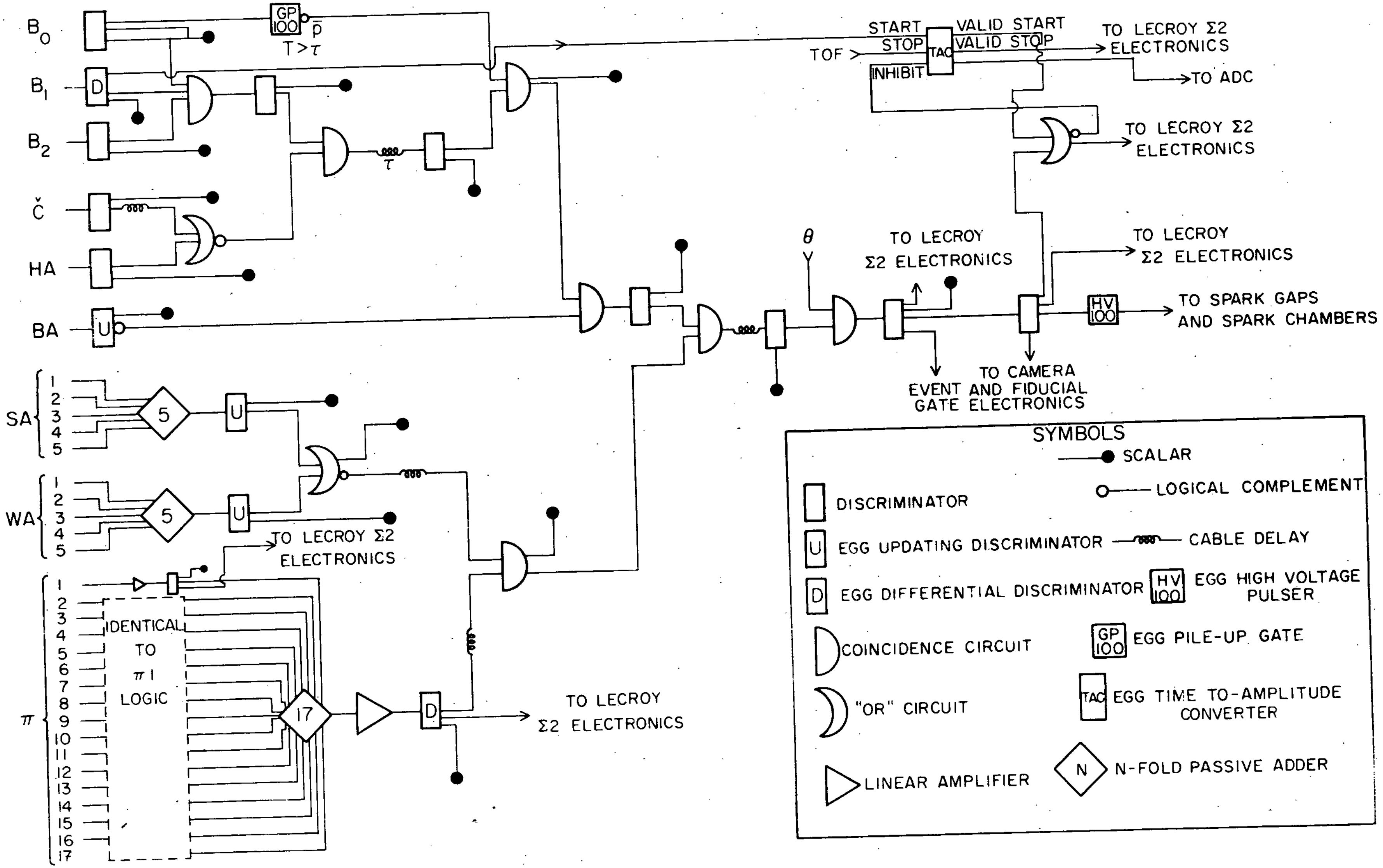

Figure III-5 Neutron Counter Logic. (Symbols are defined in figure III-4.)

NEUTRON COUNTER LOGIC (PULSE HEIGHT LOGIC NOT SHOWN)

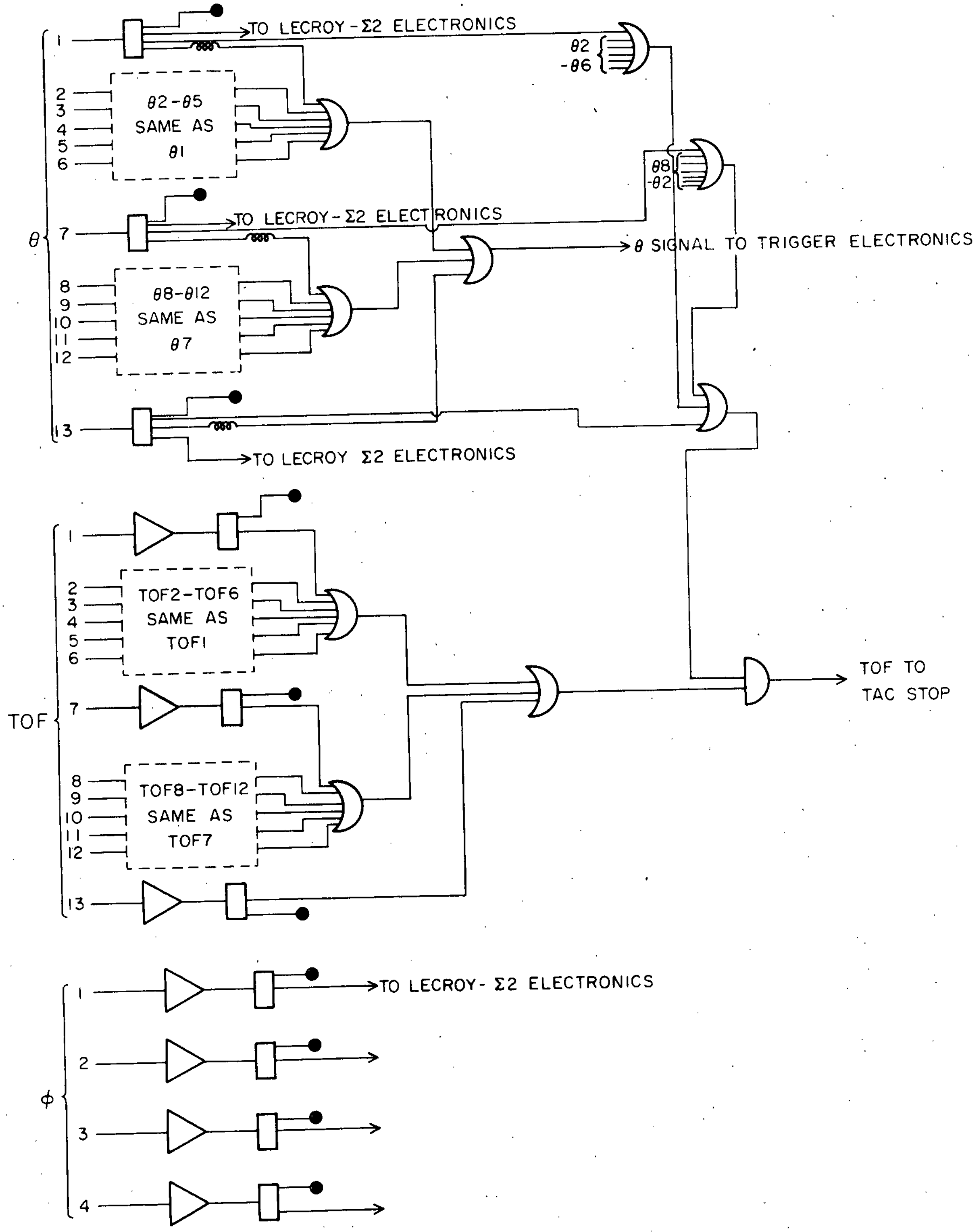

recorder was occasionally used as backup for, or in addition to, the $\Sigma 2$).

The neutron "tof" signals went through 13 individual triggers set at a low voltage-discrimination level which corresponded to ~1 MeV energy loss in the neutron counter. The neutron "θ" signals also went through a set of 13 individual triggers, but these had a higher level of discrimination which corresponded to ~6 MeV energy loss in the neutron counter. A "tof" signal in a loose coincidence with a "θ" signal was required to give the TAC a stop signal. The purpose of this high-low discrimination procedure was to minimize the effects of time slewing in the recorded time-of-flight.

The outputs of SA_{1-5} and WA_{1-5} were separately passively added giving one SA and one WA signal. The requirement of two and only two π hodoscope counts was achieved by passively adding the outputs of the 17 individual discriminators and using an EGG differential discriminator whose voltage window was then appropriately set.

D. Use of the On-Line Computer

The $\Sigma 2$ computer was programmed to store, update, and dynamically display on a CRT unit, the counts in both the neutron and pion hodoscopes, the time-of-flight spectra for the neutron θ bins, and several momentum transfer bins of missing mass spectra. The various counter displays provided an excellent monitor of the scintillation counters in supplement to the counter single count rates, which were checked hourly during the experiment.

The computer, with its high-speed data collection potential, was also used in monitoring the timing of the neutron counters. During the actual data runs the data collection rate was limited by the time needed to advance the camera. However, once every six data runs the camera and spark chambers were disabled, the timing gates on the neutron counters were modified, and the trigger electronics was changed to accept events of the type

$$\pi^- p \rightarrow \gamma + \text{anything}$$

The photons were detected in the neutron counter hodoscope, and this "prompt peak" time set the origin of the scale used to compute the neutron time-of-flight.

The Σ2 also transferred the input information for each event onto 9-track magnetic tape which was subsequently processed on the Argonne IBM 360.

E. Raw Data Analysis: Neutral Missing Mass Spectrometry

If we consider the reaction

$$\pi^- p \rightarrow \mathbf{X}^o n \tag{III.1}$$

then conservation of four momentum yields:

$$M_x^2 = m_\pi^2 - 2(E_\pi + m_p)\ T_n + 2p_\pi p_n \cos\theta \tag{III.2}$$

where we have neglected the neutron-proton mass difference and are working the laboratory frame, i.e., the proton is at rest. T_N is the kinetic

Figure III-6 Kinematics of reaction III.1 for incident momentum 3.65 GeV/c.

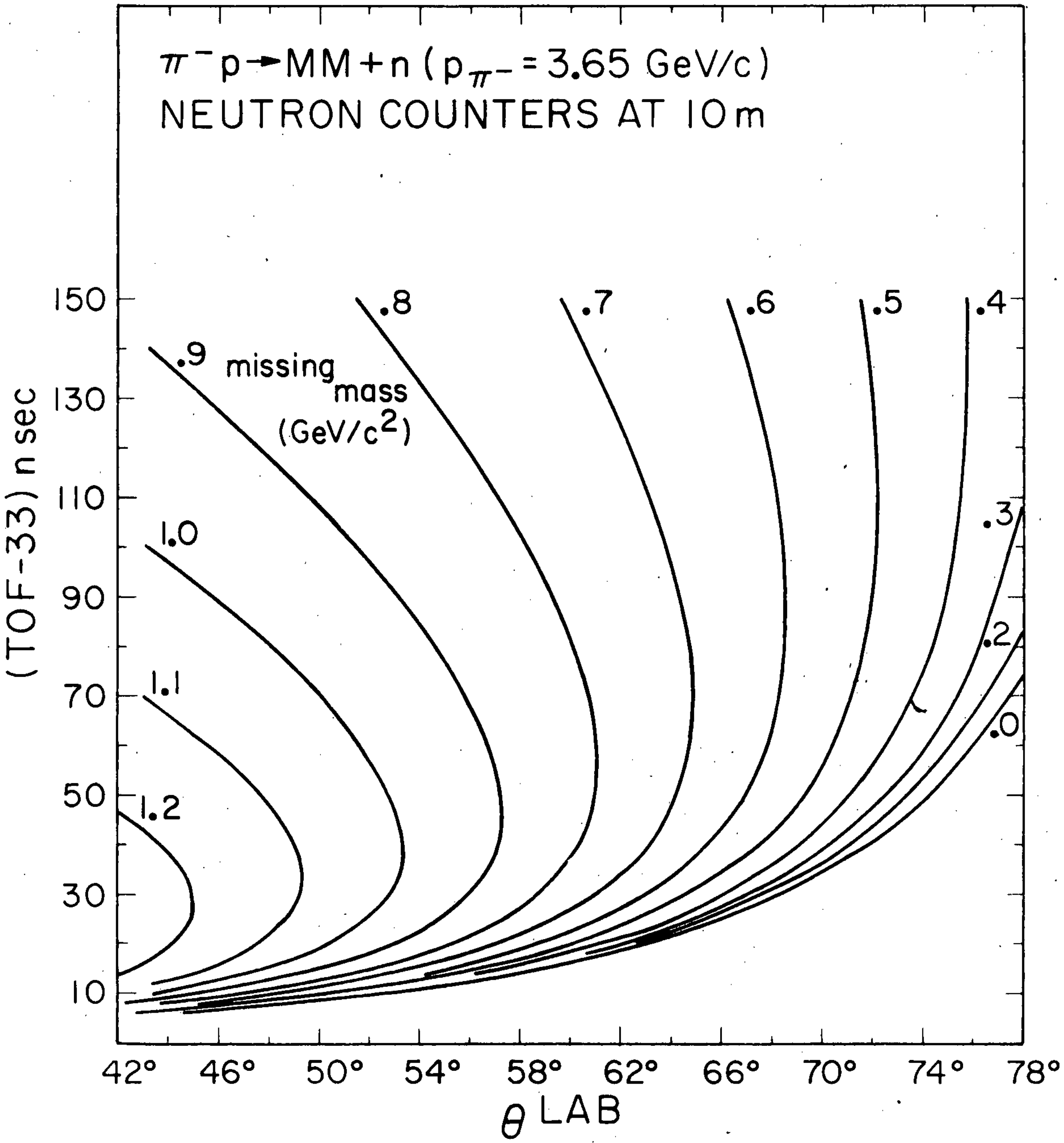
$\pi^- p \rightarrow MM + n$ (p_{π^-} = 3.65 GeV/c)
NEUTRON COUNTERS AT 10 m
.9 missing mass (GeV/c^2)
.8
.7
.6
.5
.4
.3
.2
.0
1.0
1.1
1.2
(TOF-33) nsec
150
130
110
90
70
50
30
10
42°
46°
50°
54°
58°
62°
66°
70°
74°
78°
θ LAB

Figure III-7 Kinematics of Reaction III.1 for Incident Momentum 5.5 GeV/c.

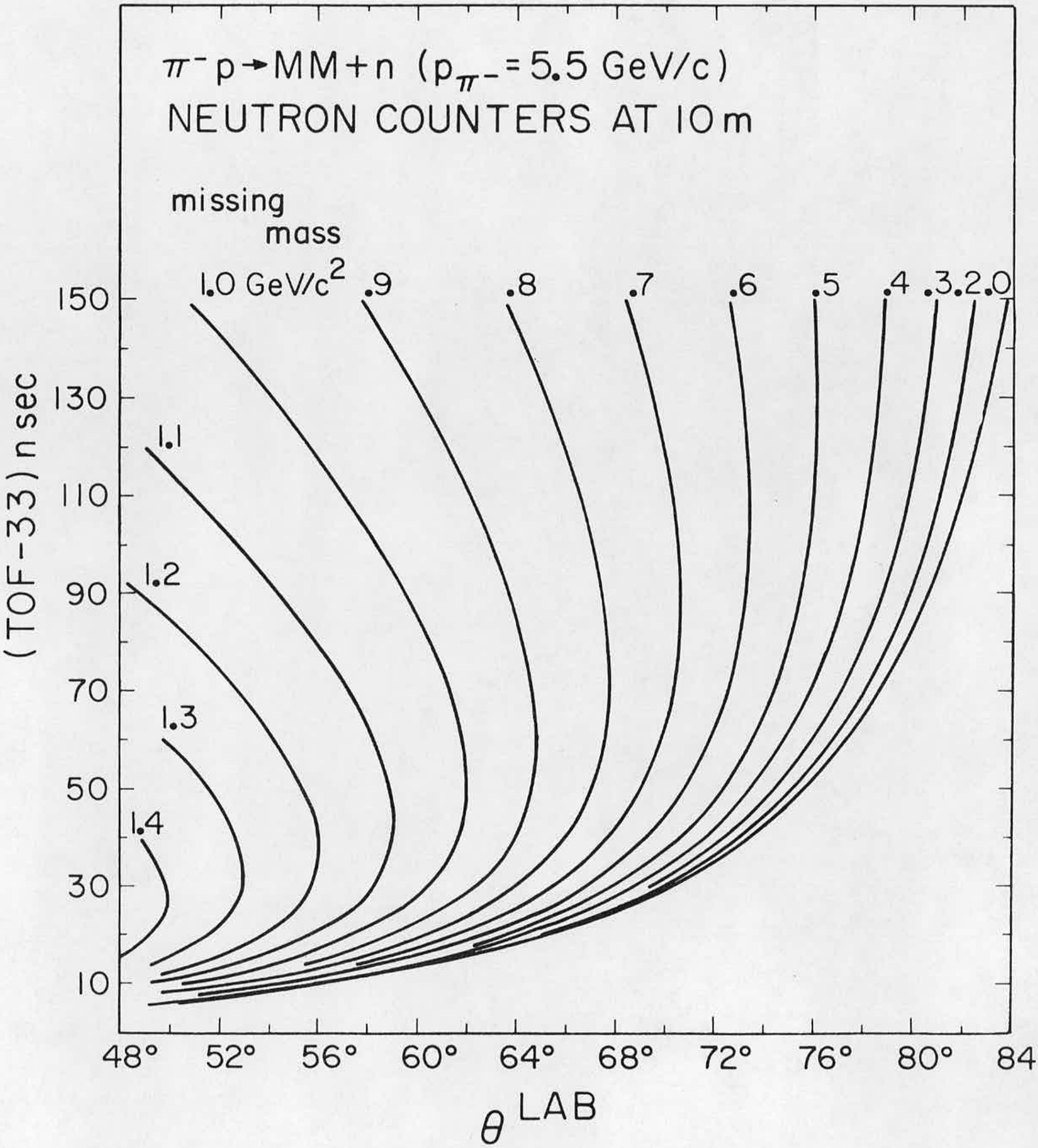
$\pi^- p \rightarrow MM + n$ ($p_{\pi^-} = 5.5$ GeV/c)
NEUTRON COUNTERS AT 10 m
missing mass
1.0 GeV/c^2
.9
.8
.7
.6
.5
.4
.3
.2
.0
1.1
1.2
1.3
1.4
(TOF-33) n sec
150
130
110
90
70
50
30
10
48°
52°
56°
60°
64°
68°
72°
76°
80°
84°
θ^{LAB}

energy of the neutron, θ_N is the angle the outgoing neutron makes with the incident pion beam, E_π is the energy of the incident pion, and p_π is it's momentum. Both the neutron's momentum, p_N, and its kinetic energy, T_N, can be expressed as single-valued functions of the neutron time-of-flight. For two of our incident beam momenta, the parametric curves of constant mass in the time-of-flight (TOF) plane are shown in figures III-6 and III-7. We note that at large neutron time-of-flight, which are equivalent to low-momentum transfer to the neutron, for a given range of theta, a rather large range of time-of-flight corresponds to a small range of mass.

Using our "on-line" information, we have a missing mass spectrometer and can find the mass of the missing neutral boson. The input parameters to the calculation are: (1) the incident beam momentum, (2) the angle of the neutron, and (3) the neutron time-of-flight. For this on-line analysis our ignorance about the position of the event vertex within the target produces errors in both the neutron angle and its time-of-flight. Another source of error in the time-of-flight comes about because of the non-incorporation of the information obtained in the "prompt peak" runs described in section III.D.

A calculation of the time-of-flight in terms of measured quantities is:

$$t = S(T^{ADC}_{event} - T^{ADC}_{prompt}) + L/C + \Delta/C \qquad (III.4)$$

where T^{ADC}_{event} and T^{ADC}_{prompt} are the TAC-ADC system channel numbers for the recorded event and for the location of the "prompt peak" in the neutron counter hit in this event, L is the distance from the target center to the center of this neutron counter in centimeters, Δ is the vector distance along the beam direction from the target center to the event vertex in centimeters, $C = 30\text{cm/nsec}$ is the speed of light, and S is the TAC-ADC scale factor in nsec/channel. In the on-line analysis, we take $\Delta = 0$ and $\frac{L}{C} - ST^{ADC}_{prompt} =$ constant for all counters, i.e., we take the event vertex at the target center and assume all the counters are in time (they were originally cabled to satisfy this timing condition) and at the same distance from the target center.

The results of the on-line analysis is shown for all three incident beam momenta for a few momentum transfer bins in figures III-8, III-9 and III-10. Because of our trigger electronics, these histograms contain all events of the type

$$\pi^- p \rightarrow n + 2 \text{ charged particles} + m \text{ neutrals}$$

and thus contain a substantial number of background events which can be eliminated, as will be discussed in Chapter IV, by scanning the film for only

$$\pi^- p \rightarrow \pi^+\pi^-\gamma n \qquad \text{or} \qquad \pi^- p \rightarrow \pi^+\pi^-\gamma\gamma n$$

candidates, i.e., those pictures showing conversion of at least one photon. This background plus the resolution problem introduced by the time-of-flight errors precludes any identification of signal above noise in the two high

Figure III-8 Raw Missing Mass $.15 < |t| < .35$ (GeV/c)^2.

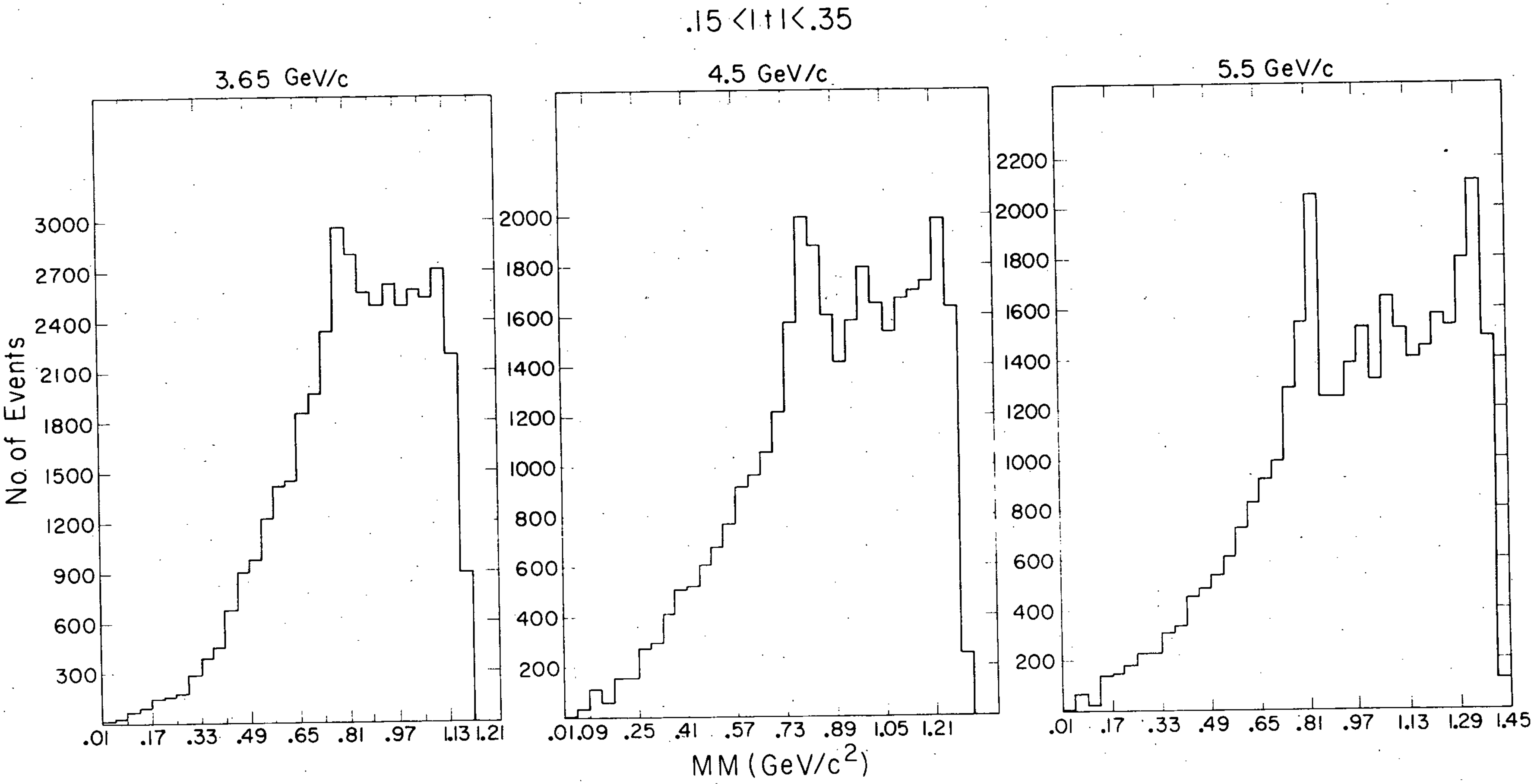
.15 < |t| < .35
3.65 GeV/c
4.5 GeV/c
5.5 GeV/c
No. of Events
300
600
900
1200
1500
1800
2100
2400
2700
3000
200
400
600
800
1000
1200
1400
1600
1800
2000
2200
.01
.17
.33
.49
.65
.81
.97
1.13
1.21
.01
.09
.25
.41
.57
.73
.89
1.05
1.21
1.29
1.45
MM (GeV/c2)

Figure III-9 Raw Missing Mass $.35 < |t| < .60$ $(\mathrm{GeV}/c)^2$.

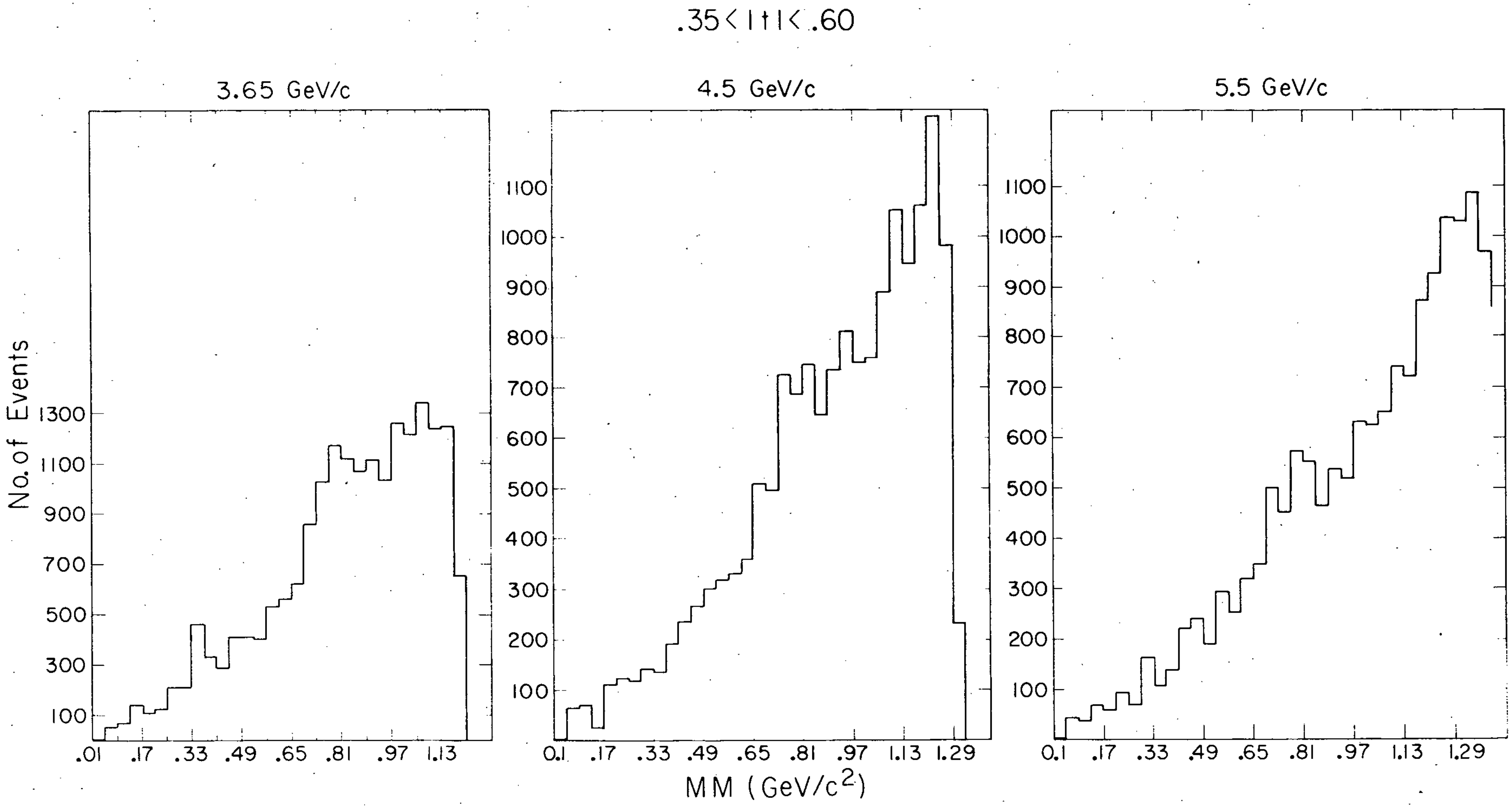
.35 < |t| < .60
3.65 GeV/c
4.5 GeV/c
5.5 GeV/c
No. of Events
100
300
500
700
900
1100
1300
100
200
300
400
500
600
700
800
900
1000
1100
.01
.17
.33
.49
.65
.81
.97
1.13
0.1
1.29
MM (GeV/c^2)

Figure III-10 Raw Missing Mass $.60 < |t| < .95\ (\mathrm{GeV}/c)^2$.

$.60 < |t| < .95$

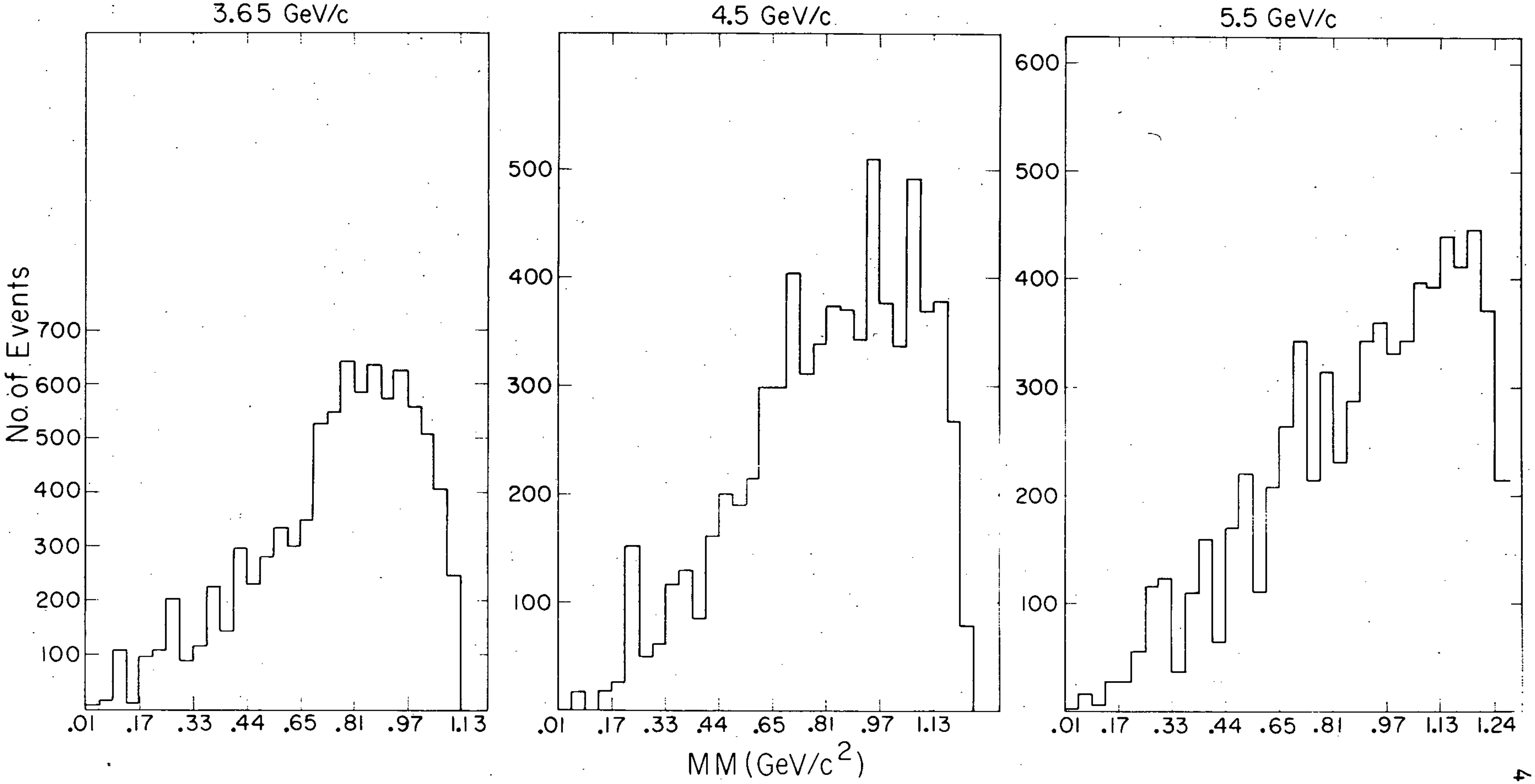
3.65 GeV/c
4.5 GeV/c
5.5 GeV/c
No. of Events
100
200
300
400
500
600
700
.01
.17
.33
.44
.65
.81
.97
1.13
1.24
MM (GeV/c^2)

momentum transfer bins, however, a signal in the ω^o mass region is visible in the lowest momentum transfer bin, $.15 \leq |t| \leq .35$ $(GeV/c)^2$. The signal's relatively narrow full width at half-maximum above background, $\Gamma \sim 80$-120 MeV/c^2, means it is not predominantly ρ(765 MeV/c^2) and is indeed an ω^o signal.

IV. EXPERIMENTAL TECHNIQUE 2: DATA REDUCTION AND ANALYSIS

A. Cuts on the Raw Data

The neutron counter timing gates, and the position of the counters relative to the target determine the acceptance of the neutral missing-mass spectrometer. (Figure IV-1 gives the acceptance for an incident pion momentum of 5.5 GeV/c). We note that at large times-of-flight, or low $|t|$, the acceptance in terms of missing mass is small. However, as we go to smaller times-of-flight, i.e., larger $|t|$, the acceptance widens and a cutting procedure to reduce the number of spark chamber pictures to be scanned becomes desirable.

Using the raw time-of-flight, the neutron laboratory scattering angle with the event vertex assumed to be at the target center, and the neutron counter timing corrections, a cut on the raw data was made. For each event an error ellipse was drawn in the θ- time-of-flight plane with semi-axes of 76 milliradians in θ and 6 nsec in time-of-flight. These errors correspond to approximately four standard deviations. After drawing this ellipse, a computer program determined whether or not the ω^o mass curve lay within the ellipse. If not, the event was excluded unless the missing mass for the event was between 540 and 1030 MeV/c^2.

The validity of this cutting procedure was checked by processing a data sample both with and without the cut. No events with missing masses in the range 560-1000 MeV/c^2 were found to be excluded by the cutting procedure. Approximately 50% of the total number of pictures were eliminated by this cut.

Figure IV-1 Acceptance of the neutron counters in the θ-time-of-flight plane at 5.5 GeV/c.

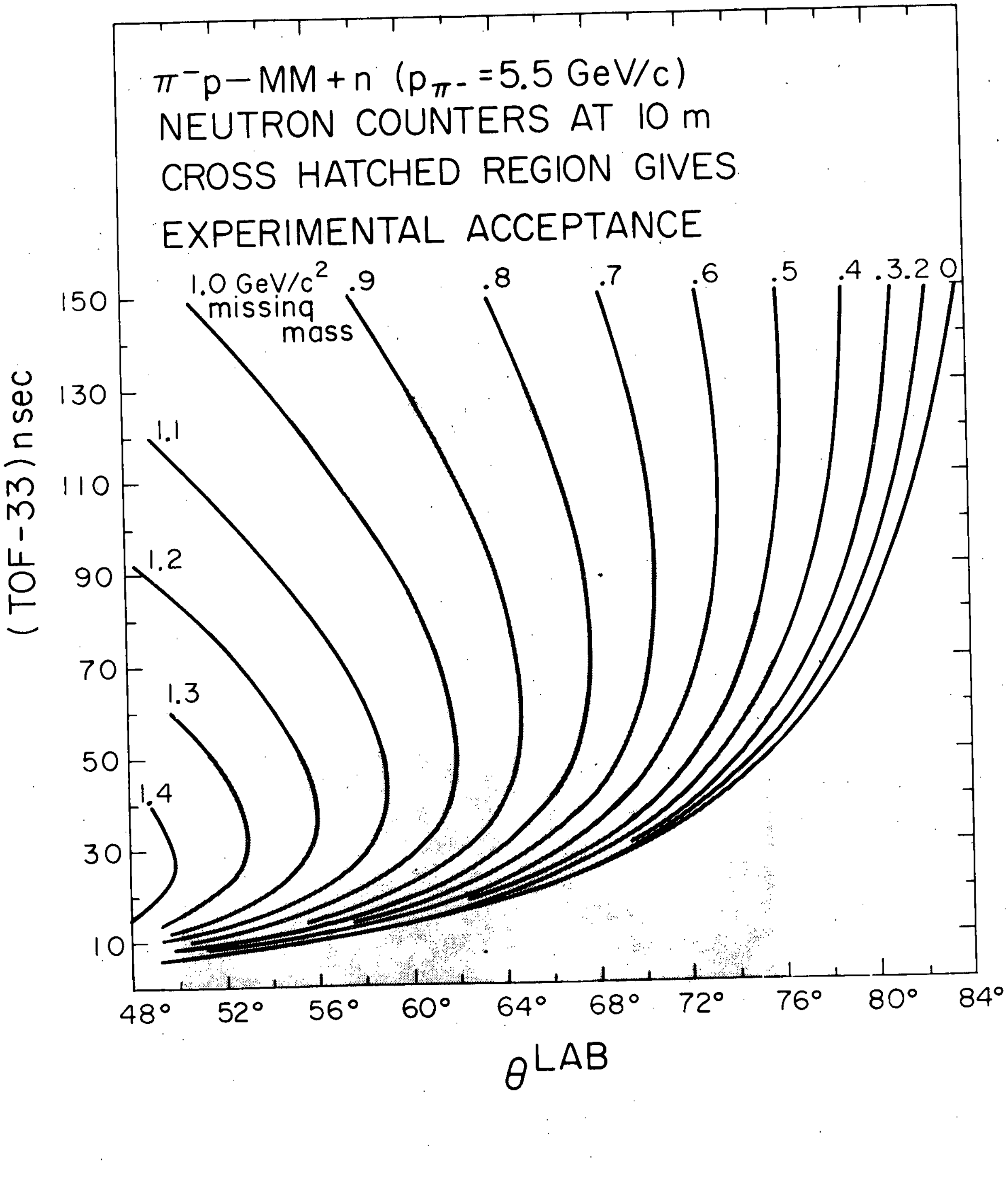
$\pi^- p - MM + n$ (p_{π^-} =5.5 GeV/c)
NEUTRON COUNTERS AT 10 m
CROSS HATCHED REGION GIVES
EXPERIMENTAL ACCEPTANCE
1.0 GeV/c^2 missing mass
.9
.8
.7
.6
.5
.4
.3
.2
0
1.1
1.2
1.3
1.4
(TOF-33) nsec
150
130
110
90
70
50
30
10
48°
52°
56°
60°
64°
68°
72°
76°
80°
84°
θ^{LAB}

In our final data plots, missing masses outside 560-1000 MeV/c^2 occur for two reasons: (1) some of the data were processed without going through the cut, and (2) at short times-of-flight the spacing between missing-mass curves in the θ-time-of-flight plane is so small that often one cannot cut without excluding events whose fitted missing mass will lie within the desired region, i.e., the error ellipse contains a wide range of allowed missing-masses.

B. Scanning and Measuring Techniques

The events passing the cutting procedure were visually scanned, and grouped into five classes: (1) chamber breakdowns, (2) events containing no γ conversion showers, (3) events containing one such shower, (4) events containing two such showers, and (5) events containing three or more such showers. For the purposes of the scan, a shower was defined to have at least five visible sparks in both the top and side views, no sparks in the thin foil chambers, and it was not allowed to point back to a secondary interaction. Additional criteria allowed the scanners to distinguish charged particles which missed the thin foil chambers from γ conversion showers. The efficiency of the scanners in identifying the ω^o candidates, i.e., the one and two shower events, will be discussed elsewhere.[19] In what follows we shall only consider the events identified as containing two conversion showers.

After being scanned the ω^o events went through another stage of filtering by the measuring personnel. The filtering eliminated events that were improperly classified by the scanners, events with an interaction vertex not in the area of our liquid Hydrogen target, and events whose topology in the reprojected image planes made measurement impossible. The ratio of events passing to events failing was ~.75-.80. (Exact figures will be given in another report[19]).

The two-photon events still surviving were measured on a University of Illinois SMP.[20] The measurement digitized the reprojected image plane positions of a set of four electroluminescent fiducial cross-hairs, the top and side view coordinates of the sparks in the two charged particle tracks, and the top and side view coordinates of the initial spark in each of the two showers. On the average a total of 20 two shower scanned events were handled by the measurers in an hour.

C. Event Reconstruction

A least squared fitting procedure was used to spatially reconstruct the events. The parameters for the optical transformation necessary in doing this fit were determined with a set of 120 fiducial cross-hairs located on the spark chambers, which were surveyed relative to the beam line. These cross-hairs were photographed once every 100 frames (as were the electroluminescent cross-hairs which were also fired on every frame.) The parameters describing the transformation from real space to the film plane were found after measuring the positions of these 120 fiducials on a film plane digitizer. The additional parameters describing the transformation from the SMP measuring plane to the film plane were independently determined bi-weekly during the period when the measurements were made.

After transforming to the fiducial plane projections of the measured sparks, a 3-dimensional least squared fit was attempted. The interaction of the two charged particle tracks located the event vertex, and the positions of the initial spark in each shower and the neutron counter position enabled the fitting program to determine the directions of all the particles in real space. The output of this computer program consisted of direction cosines for all five outgoing tracks and the coordinates of the vertex.

The direction cosines for all the outgoing tracks, the neutron time-of-flight as given by equation III.3, and the incident beam momenta were used as input to another least squares fitting program. A 1 constraint fit to the hypothesis

$$\pi^- p \rightarrow \pi^+ \pi^- \pi^o n \qquad \text{(IV.1)}$$

was then made, and the results can be seen in figures IV-2, IV-3, and IV-4, where the missing mass (X^o mass) for the reaction

$$\pi^- p \rightarrow X^o n$$

is plotted. Three plots are made at each incident beam momentum. For events which fail to kinematically fit, $\chi^2 > 16$, the missing mass is calculated using the neutron time-of-flight and angles, and the vertex position. For events which fit a subclass called "good" events is defined.

"Good" events have: (1) $\chi^2 > 16$, (2) a vertex within the target, (3) photon energies ≥ 80 MeV, and (4) agreement for the charged tracks between the projected vertical coordinates in the plane of the π hodoscope and the positions of the two π counters which were triggered during the event. For the "good" events, two missing mass histograms were plotted for each energy. The first histogram gives the spectrometer mass as determined using only the neutron counter information and vertex position. The second histogram shows the final tripion mass determined by the least squares fit to hypothesis IV.1.

In each of the histograms of "good" events, a strong signal in the ω^o mass region is visible and the width is in agreement with the expected mass resolution of the neutral missing mass spectrometer (~70 MeV/c^2 averaged over all t). For the purpose of the following analysis a straight line is drawn through the background near the ω^o mass. Our ω^o mass region is defined to be 750-830 MeV/c^2 and 80 MeV/c^2 control regions are selected on either sides of this ω^o region.

An indication of the purity of our ω^o sample can be found using the decay matrix element

$$M \sim \vec{\epsilon} \cdot \vec{p}_{\pi^+} \times \vec{p}_{\pi^-}$$

where $\vec{\epsilon}$ is the ω^o polarization vector, $\vec{p}_{\pi^+}$ and $\vec{p}_{\pi^-}$ are the charged pion 3-momenta in the ω^o rest frame. Assuming no background, the distribution of events on the Dalitz plot will be

$$\frac{dN}{d\delta} \sim \delta$$

where

Figure IV-2 Missing mass results at 3.65 GeV/c.

2

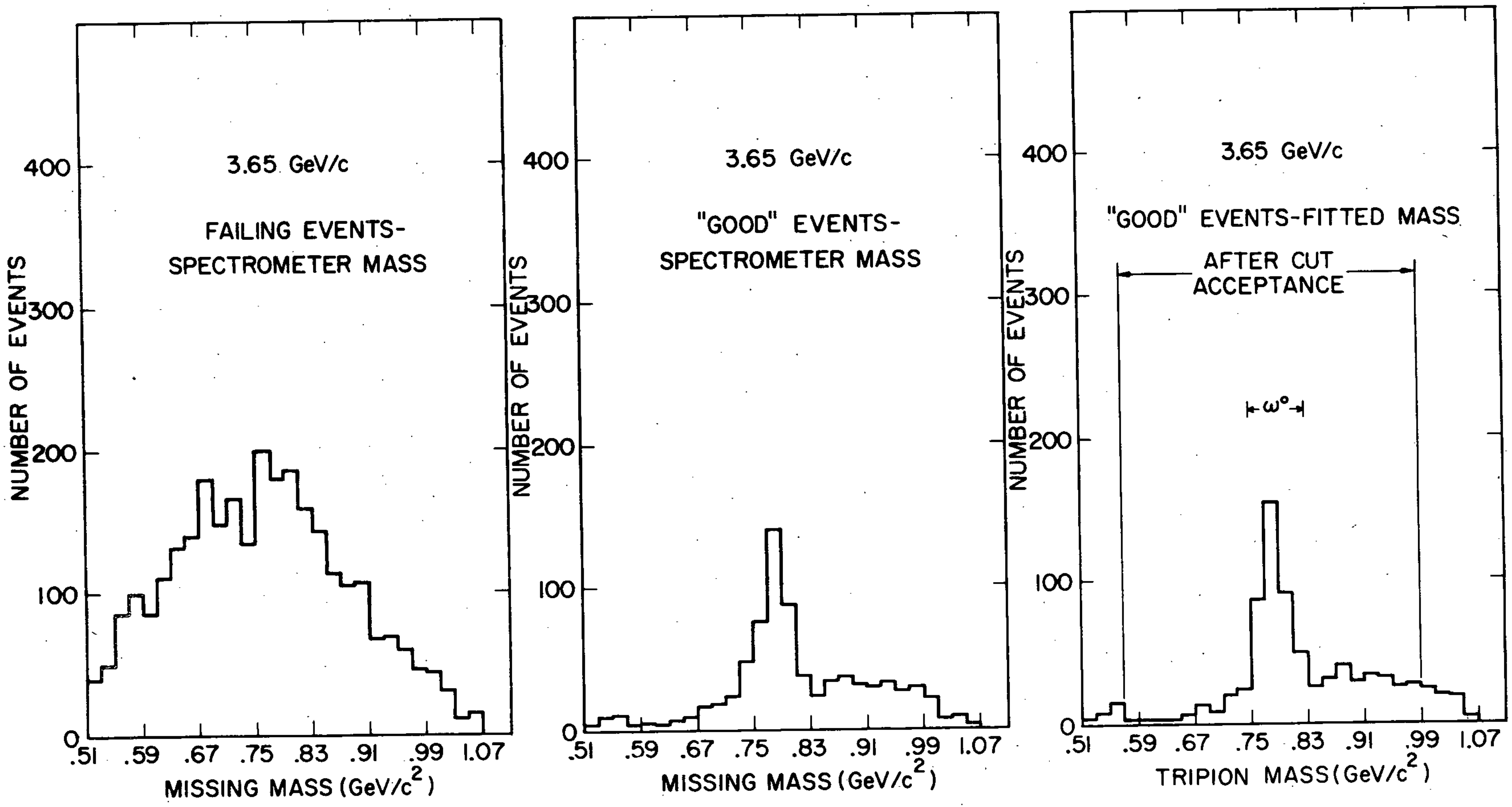
3.65 GeV/c
FAILING EVENTS-
SPECTROMETER MASS
NUMBER OF EVENTS
0
100
200
300
400
.51
.59
.67
.75
.83
.91
.99
1.07
MISSING MASS (GeV/c^2)
3.65 GeV/c
"GOOD" EVENTS-
SPECTROMETER MASS
NUMBER OF EVENTS
0
100
200
300
400
.51
.59
.67
.75
.83
.91
.99
1.07
MISSING MASS (GeV/c^2)
3.65 GeV/c
"GOOD" EVENTS-FITTED MASS
AFTER CUT
ACCEPTANCE
ω^o
NUMBER OF EVENTS
0
100
200
300
400
.51
.59
.67
.75
.83
.91
.99
1.07
TRIPION MASS (GeV/c^2)

Figure IV-3 Missing mass results at 4.5 GeV/c.

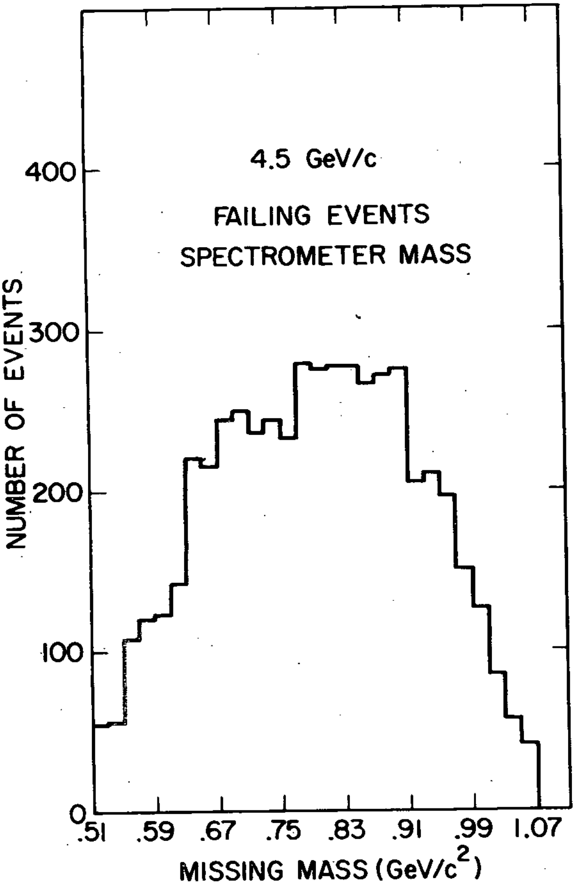
4.5 GeV/c
FAILING EVENTS
SPECTROMETER MASS
NUMBER OF EVENTS
0
100
200
300
400
.51
.59
.67
.75
.83
.91
.99
1.07
MISSING MASS (GeV/c^2)

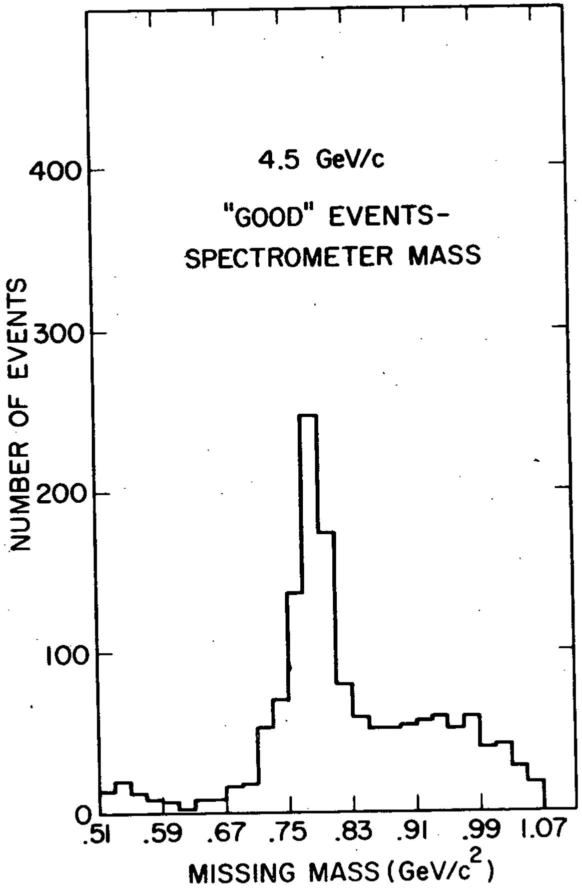
4.5 GeV/c
"GOOD" EVENTS-
SPECTROMETER MASS
NUMBER OF EVENTS
0
100
200
300
400
.51
.59
.67
.75
.83
.91
.99
1.07
MISSING MASS (GeV/c^2)

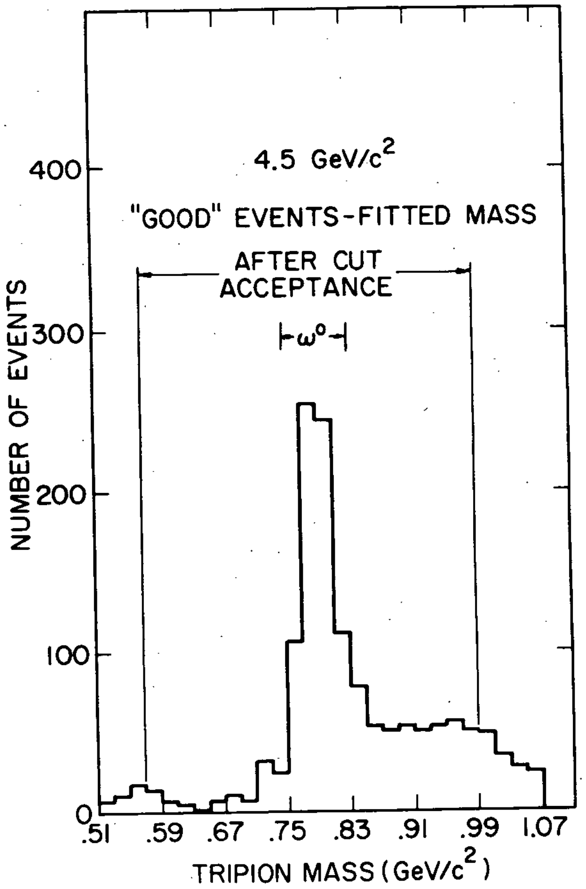
4.5 GeV/c^2
"GOOD" EVENTS-FITTED MASS
AFTER CUT
ACCEPTANCE
ω^0
NUMBER OF EVENTS
0
100
200
300
400
.51
.59
.67
.75
.83
.91
.99
1.07
TRIPION MASS (GeV/c^2)

Figure IV-4 Missing mass results at 5.5 GeV/c.

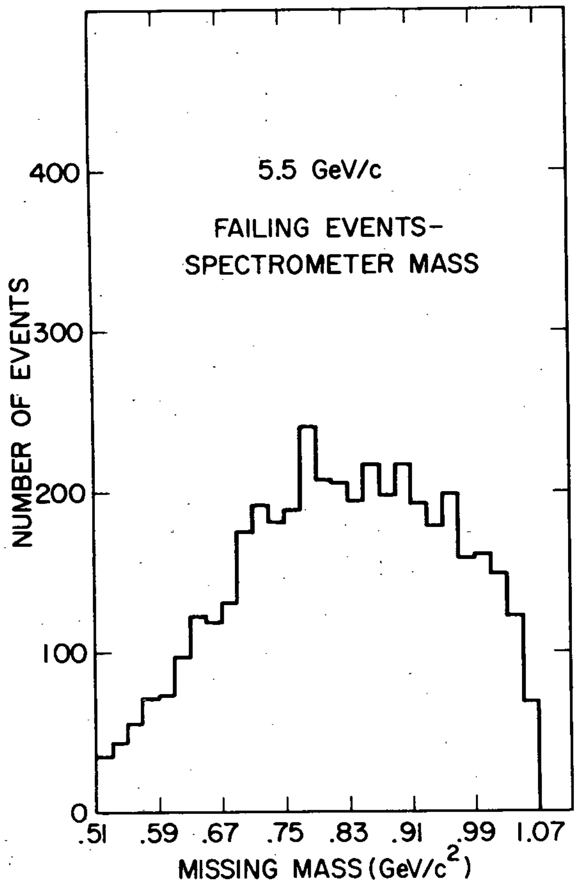
5.5 GeV/c
FAILING EVENTS-
SPECTROMETER MASS
NUMBER OF EVENTS
0
100
200
300
400
.51
.59
.67
.75
.83
.91
.99
1.07
MISSING MASS (GeV/c^2)

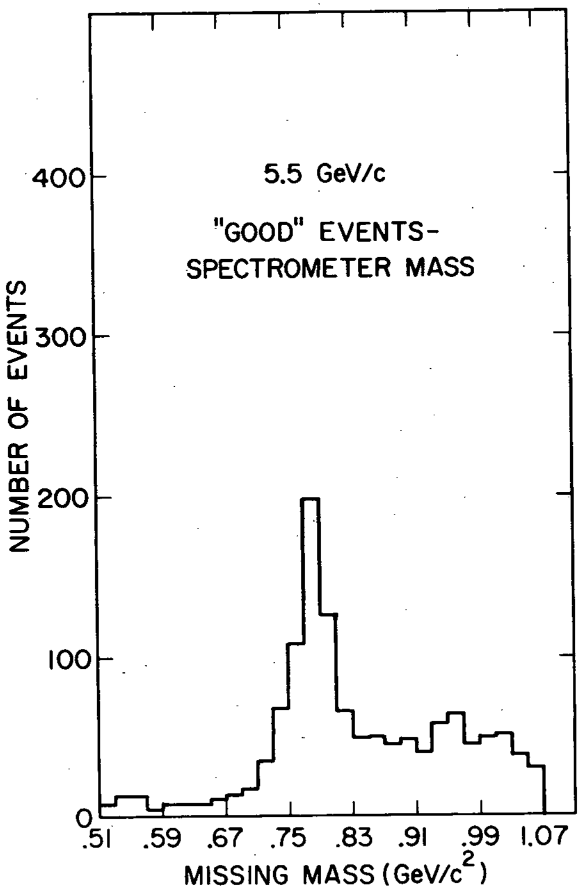
5.5 GeV/c
"GOOD" EVENTS-
SPECTROMETER MASS
NUMBER OF EVENTS
0
100
200
300
400
.51
.59
.67
.75
.83
.91
.99
1.07
MISSING MASS (GeV/c^2)

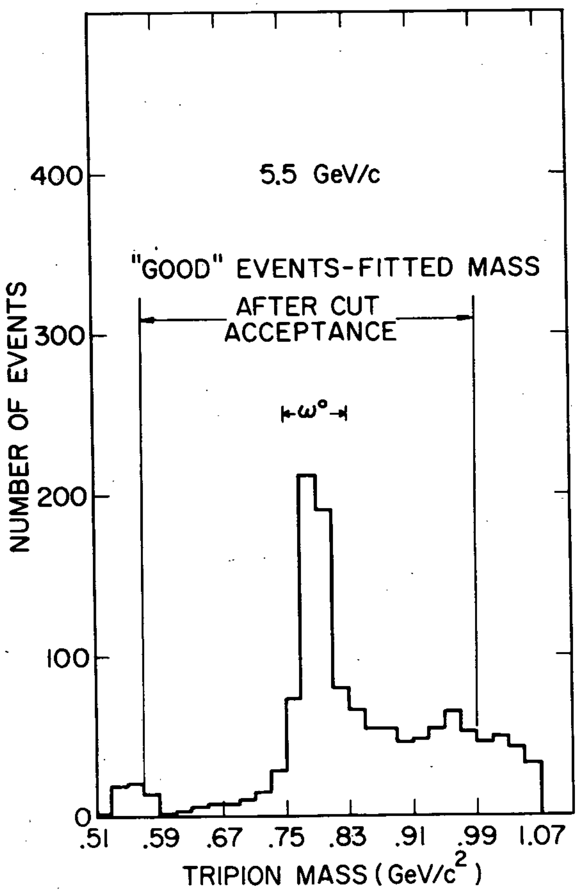
5.5 GeV/c
"GOOD" EVENTS-FITTED MASS
AFTER CUT
ACCEPTANCE
ω°
NUMBER OF EVENTS
0
100
200
300
400
.51
.59
.67
.75
.83
.91
.99
1.07
TRIPION MASS (GeV/c^2)

$$\delta = \left[\frac{|\vec{p}_{\pi^+} \times \vec{p}_{\pi^-}|}{|\vec{p}_{\pi^+} \times \vec{p}_{\pi^-}|_{max}} \right]^2$$

and $|\vec{p}_{\pi^+} \times \vec{p}_{\pi^-}|^2$ is a maximum at the center of the Dalitz plot. In figures IV-5, IV-6 and IV-7 we plot number of events vs. δ after making a background subtraction. The agreement of the data with the theoretical prediction of a straight line, is good, and a study of the control regions shows no evidence of such behavior for the background.

D. Experimental Biases

Two possible sources of bias must be examined before calculating spin-density matrix elements as a function of t. The geometric acceptance of the detection apparatus is one source of bias. High statistics Monte-Carlo event simulation shows that for unpolarized ω^o's, the "good" 28 events detected simulate some slight polarization. (We use the term "good" events as defined in section IV.C). A weighting function of the form

$$W = \left[\sum_{L=o}^{3} \sum_{M=-L}^{L} a_M^L Y_L^M(\theta,\varphi) \right]^{-1}$$

where the coefficients of the spherical harmonics, the a_M^L, are to be determined, is applied to the Monte Carlo events in an effort to remove this bias.

$$W = (.1 + .02 \cos^2\theta + .21 \sin^2\theta\cos 2\varphi)^{-1} \qquad \text{(IV.2)}$$

Figure IV-5 Radial Dalitz plot density at 3.65 GeV/c.

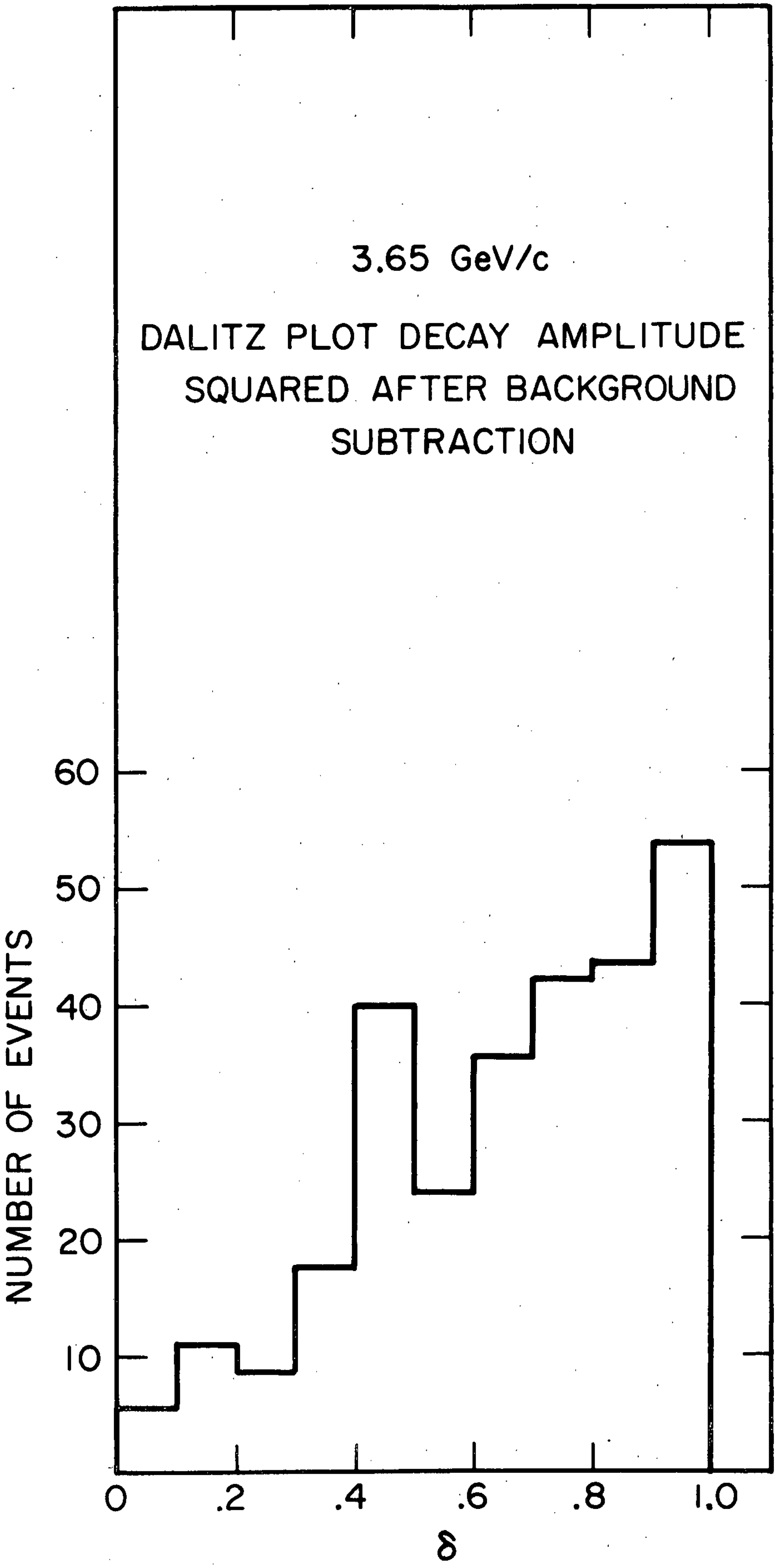
3.65 GeV/c
DALITZ PLOT DECAY AMPLITUDE SQUARED AFTER BACKGROUND SUBTRACTION
NUMBER OF EVENTS
60
50
40
30
20
10
0
.2
.4
.6
.8
1.0
δ

Figure IV-6 Radial Dalitz plot density at 4.5 GeV/c.

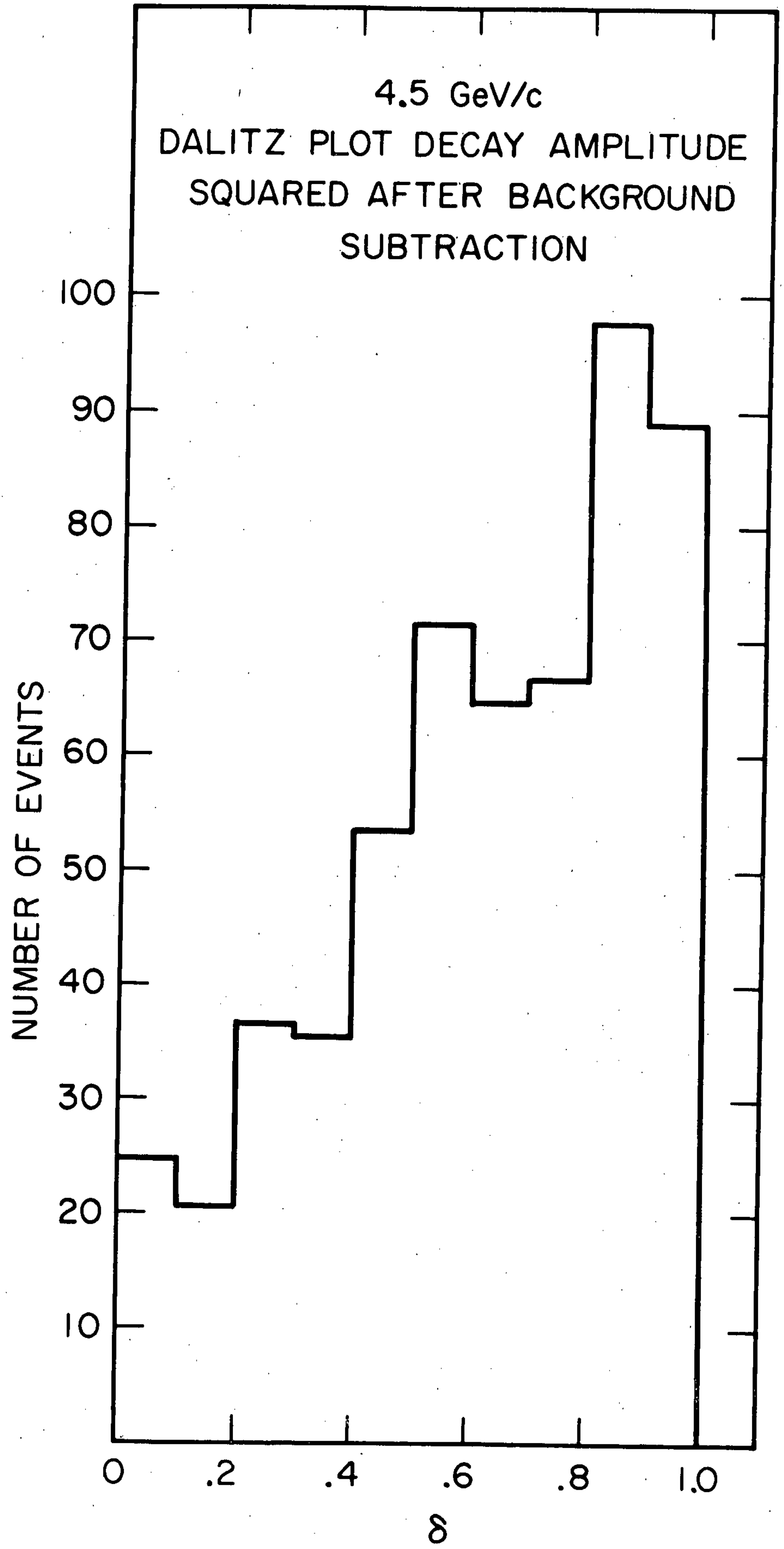
4.5 GeV/c
DALITZ PLOT DECAY AMPLITUDE SQUARED AFTER BACKGROUND SUBTRACTION
NUMBER OF EVENTS
100
90
80
70
60
50
40
30
20
10
0
.2
.4
.6
.8
1.0
δ

Figure IV-7 Radial Dalitz plot density at 5.5 GeV/c.

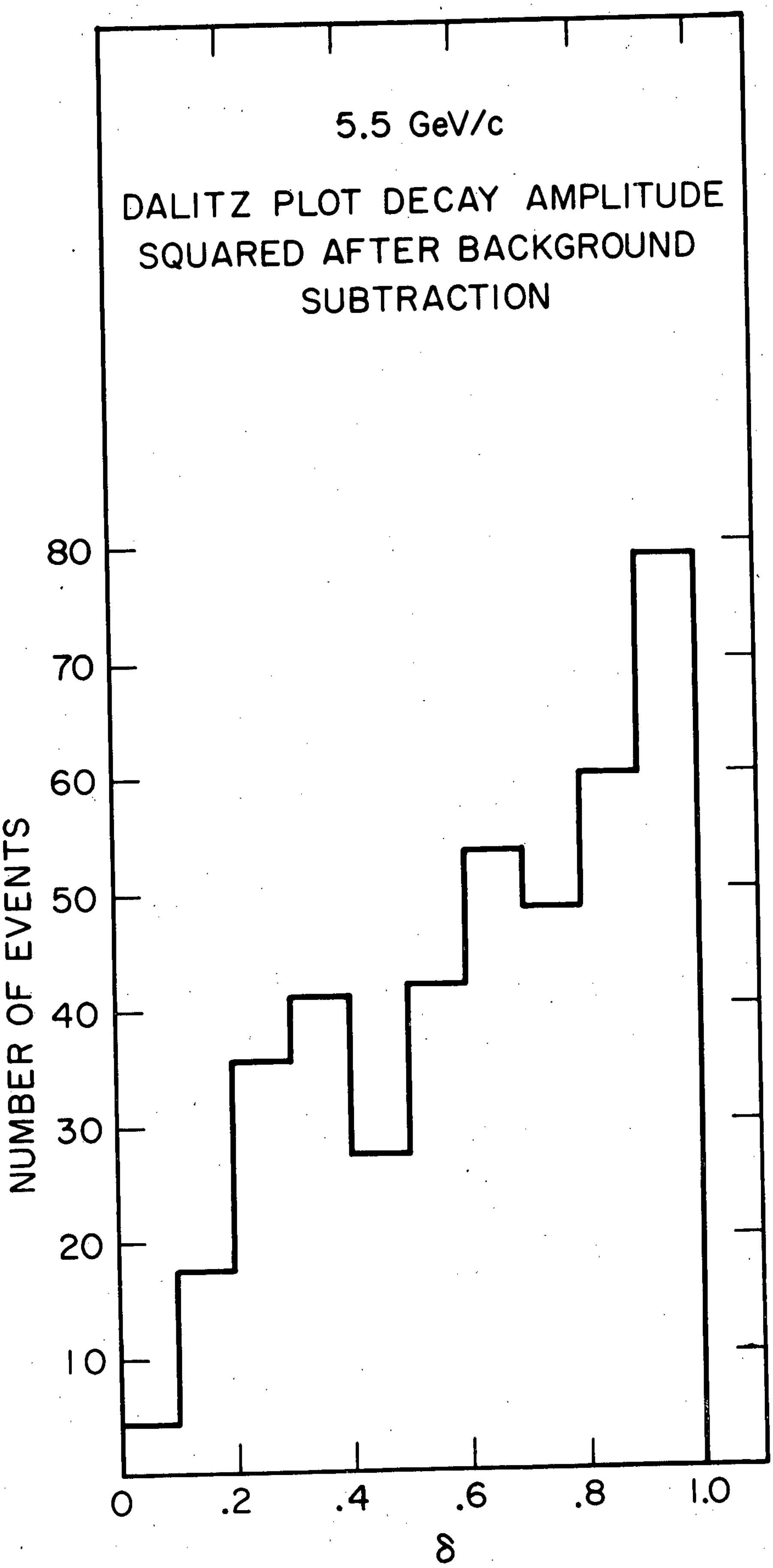
5.5 GeV/c
DALITZ PLOT DECAY AMPLITUDE SQUARED AFTER BACKGROUND SUBTRACTION
NUMBER OF EVENTS
10
20
30
40
50
60
70
80
0
.2
.4
.6
.8
1.0
δ

is found to be an adequate representation of the weighting function at all three incident momenta. The projections of the angular distributions for Monte-Carlo events using this weighting technique are shown in figures IV-8, IV-9, and IV-10. All are in good agreement with straight line predictions of an unpolarized ω^o. In addition, the density matrix elements are calculated for these events, and we find

$$\begin{array}{rcl l}
\rho_{oo} & = & .335 \pm .016 & \\
\rho_{1-1} & = & -.009 \pm .013 & \text{at } 3.65 \text{ GeV/c} \\
\text{Re}\rho_{10} & = & -.009 \pm .007 & \\
 & & & \\
\rho_{oo} & = & .349 \pm .015 & \\
\rho_{1-1} & = & .009 \pm .012 & \text{at } 4.5 \text{ GeV/c} \\
\text{Re}\rho_{10} & = & .009 \pm .007 & \\
 & & & \\
\rho_{oo} & = & .362 \pm .015 & \\
\rho_{1-1} & = & .002 \pm .012 & \text{at } 5.5 \text{ GeV/c} \\
\text{Re}\rho_{10} & = & .009 \pm .006 &
\end{array}$$

These are to be compared with the input values of $\rho_{oo} = 1/3$, $\rho_{1-1} = 0$, and $\text{Re}\rho_{10} = 0$. We conclude that the weight given in equation IV.2 removes the geometric bias of our equipment.

The other course of bias involves the background. Our background consists of 3π non-resonating events and non-3π random background events. The latter background consists mainly of events distributed uniformly in neutron time-of-flight and thus is concentrated at low $|t|$. The removal of this random background is in principle accomplished by the least squares

Figure IV-8 Monte-Carlo angular distributions after weighting at 3.65 GeV/c.

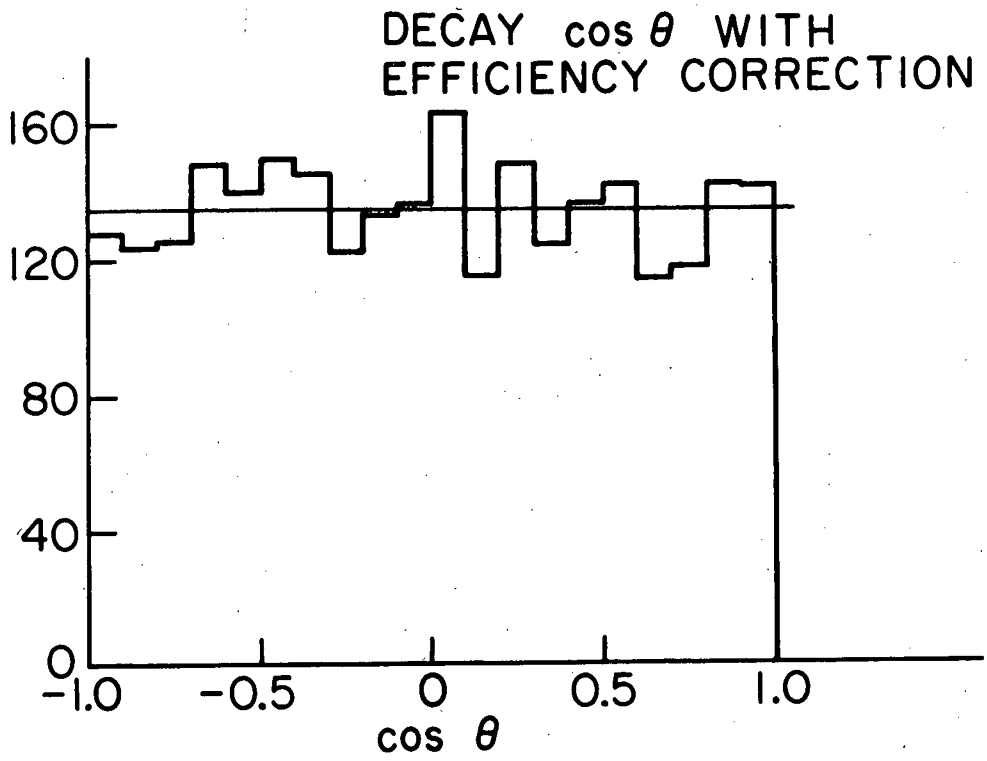
DECAY cos θ WITH
EFFICIENCY CORRECTION
160
120
80
40
0
−1.0
−0.5
0
0.5
1.0
cos θ

3.65 GeV/c

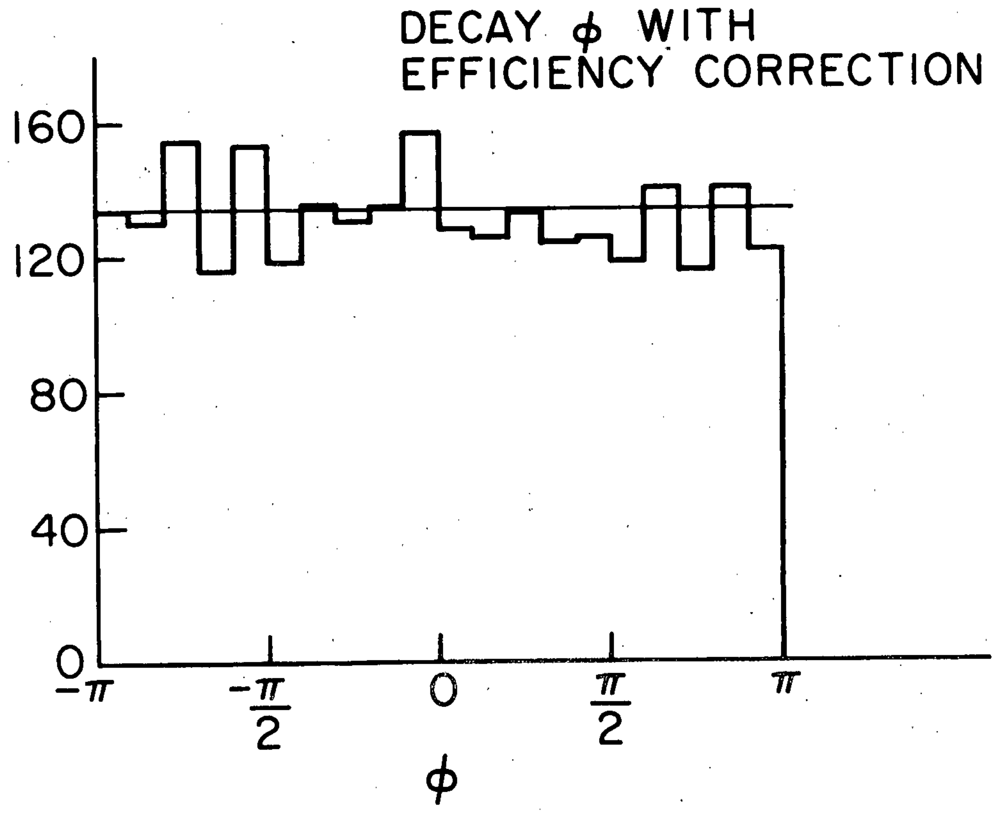
DECAY φ WITH
EFFICIENCY CORRECTION
160
120
80
40
0
−π
−π/2
0
π/2
π
φ

Figure IV-9 Monte-Carlo angular distributions after weighting at 4.5 GeV/c.

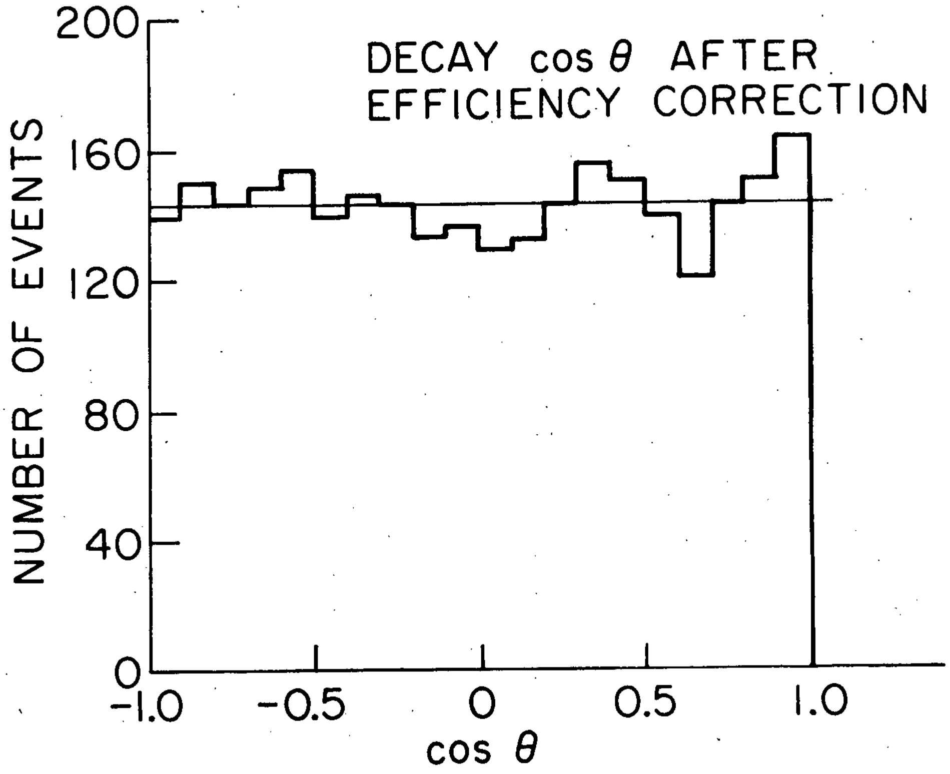
DECAY cos θ AFTER
EFFICIENCY CORRECTION
NUMBER OF EVENTS
200
160
120
80
40
0
-1.0
-0.5
0
0.5
1.0
cos θ

4.5 GeV/c

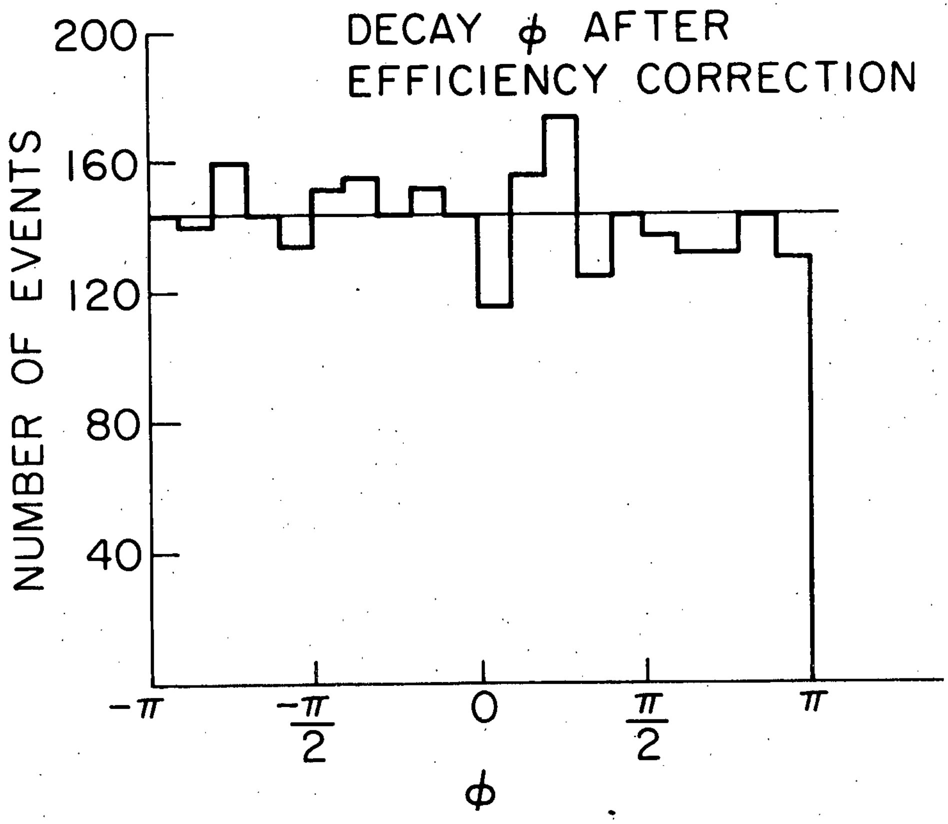
DECAY φ AFTER
EFFICIENCY CORRECTION
NUMBER OF EVENTS
200
160
120
80
40
−π
−π/2
0
π/2
π
φ

Figure IV-10 Monte-Carlo angular distributions after weighting at 5.5 GeV/c.

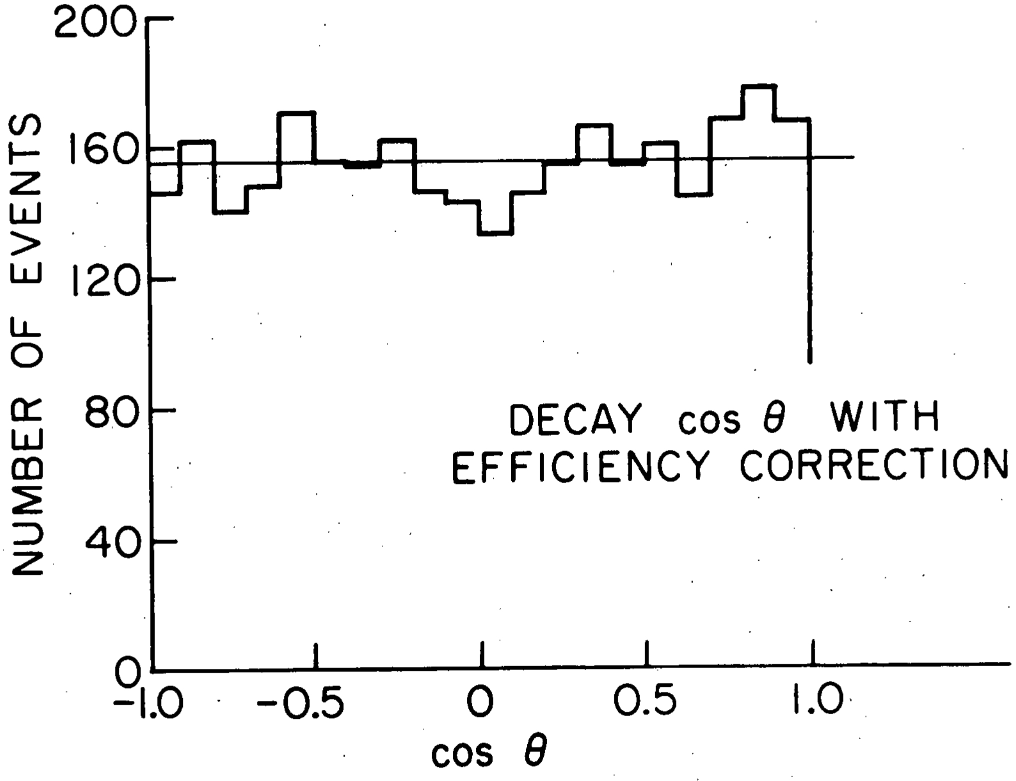
DECAY cos θ WITH
EFFICIENCY CORRECTION
NUMBER OF EVENTS
200
160
120
80
40
0
-1.0
-0.5
0
0.5
1.0
cos θ

5.5 GeV/c

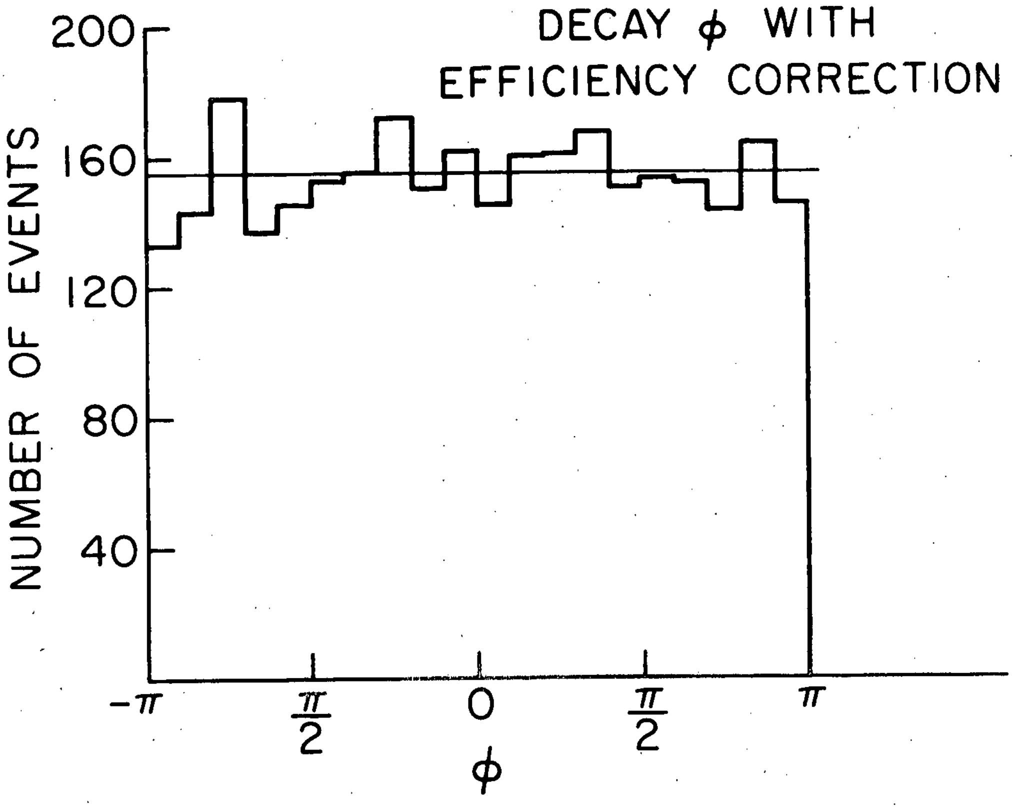
DECAY φ WITH
EFFICIENCY CORRECTION
NUMBER OF EVENTS
200
160
120
80
40
−π
π/2
0
π/2
π
φ

fitting program, however, there is evidence that some fraction survives, especially in the 3.65 GeV/c data. In figures IV-11, IV-12, and IV-13, we have plotted the distribution of event vertices in the target along the beam direction. The prediction of the Monte-Carlo for ω^o events is a flat distribution. At all three energies, the failing events show a peaking in the downstream direction indicative of wide angle events. The "good" events at 4.5 and 5.5 GeV/c flatten out in agreement with the Monte-Carlo, which we assume implies a flat distribution for 3π events. For the 3.65 GeV/c data, it is necessary to make the ω^o mass cut before the flattening is visible. We conclude the 3.65 GeV/c data contain some random non-3π background, and emphasize the effect is concentrated in the low $|t|$ region.

Figure IV-11 Target profile along the beam direction for failing events.

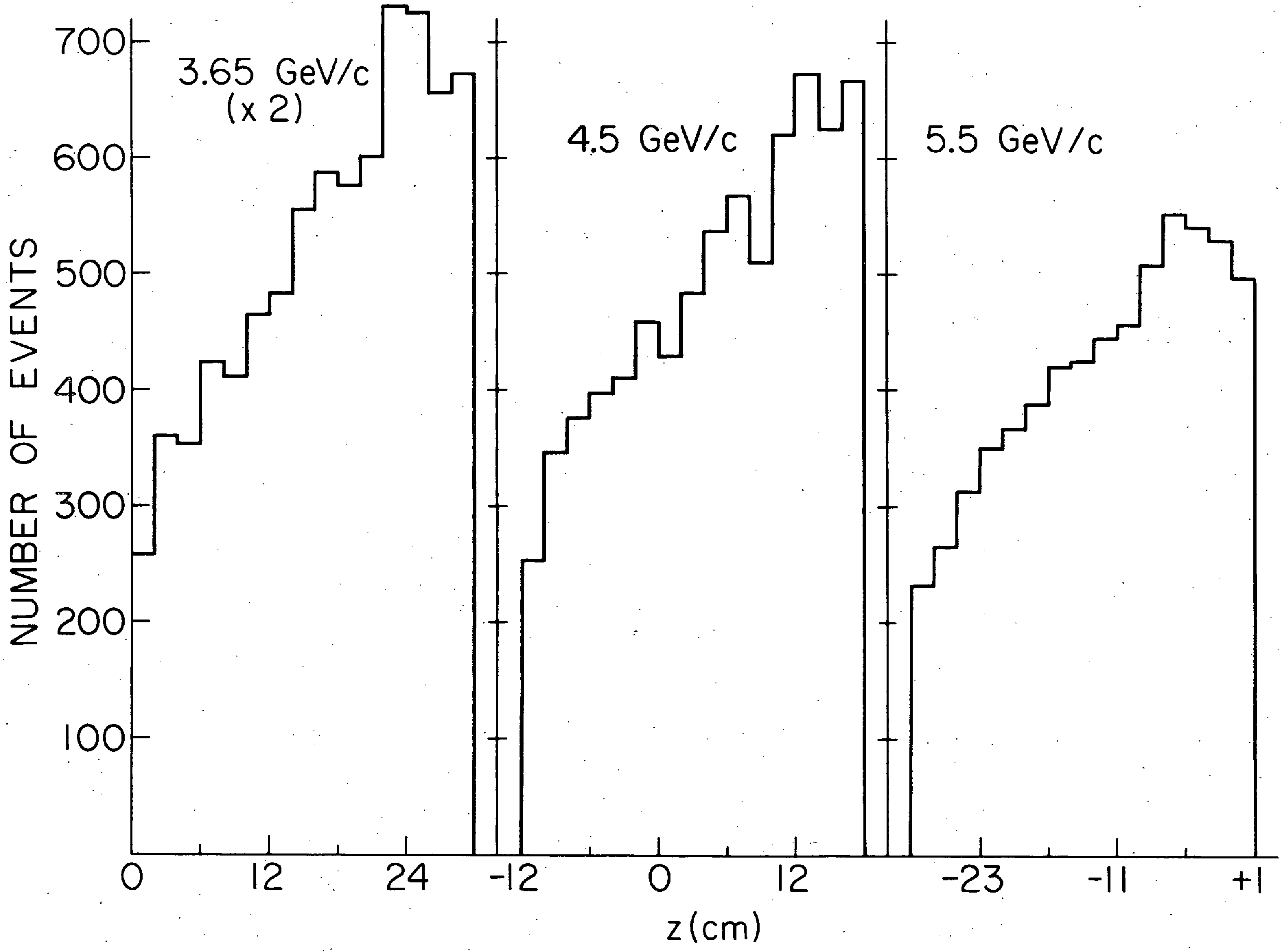
NUMBER OF EVENTS
700
600
500
400
300
200
100
3.65 GeV/c
(x 2)
4.5 GeV/c
5.5 GeV/c
0
12
24
-12
0
12
-23
-11
+1
z (cm)

Figure IV-12 Target profile along the beam direction for "good" events.

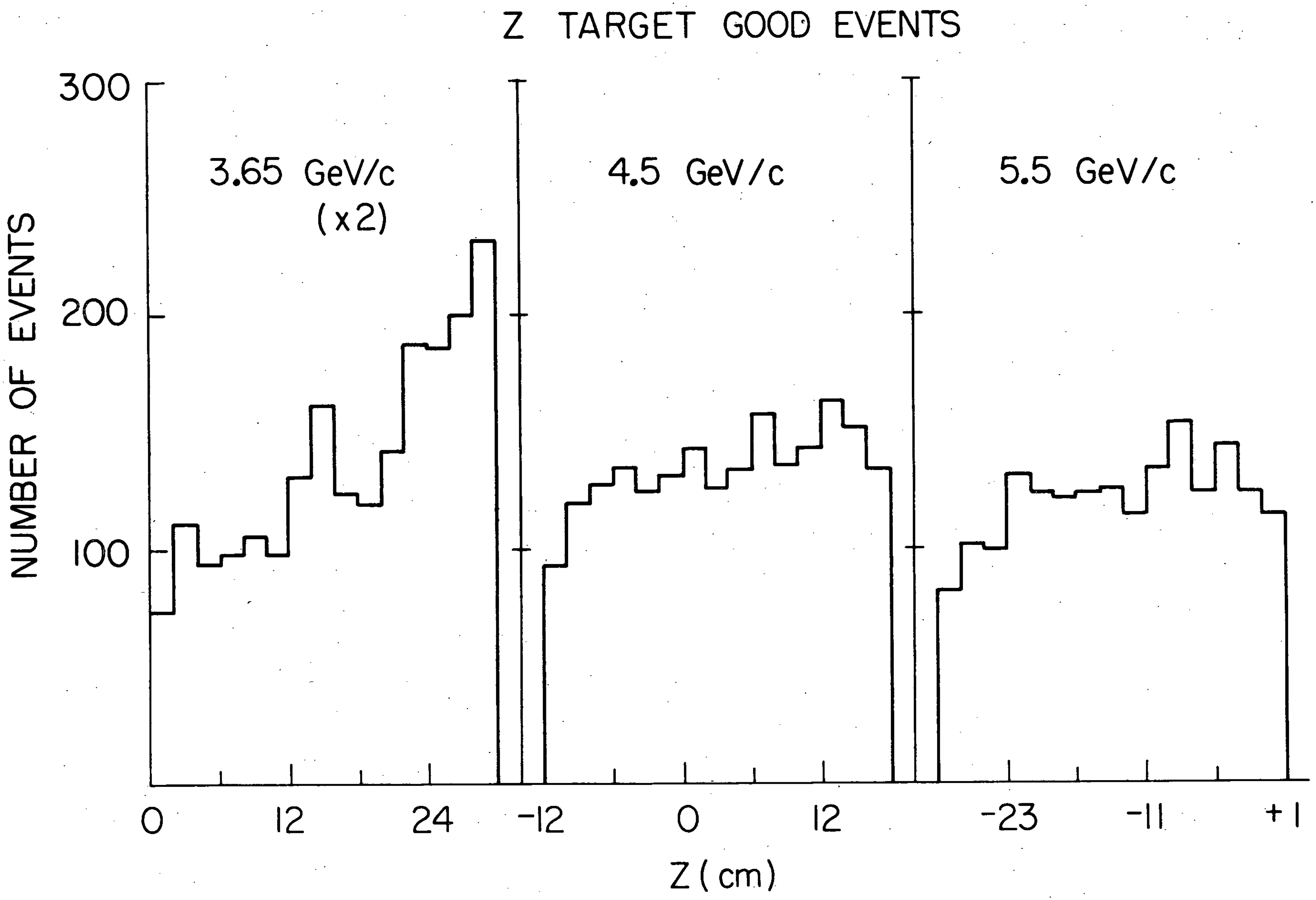

Z TARGET GOOD EVENTS
300
200
100
NUMBER OF EVENTS
3.65 GeV/c
(x2)
4.5 GeV/c
5.5 GeV/c
0
12
24
-12
0
12
-23
-11
+1
Z (cm)

Figure IV-13 Target profile along the beam direction for "good" events in the ω^o mass region (.750 - .830 MeV/c^2).

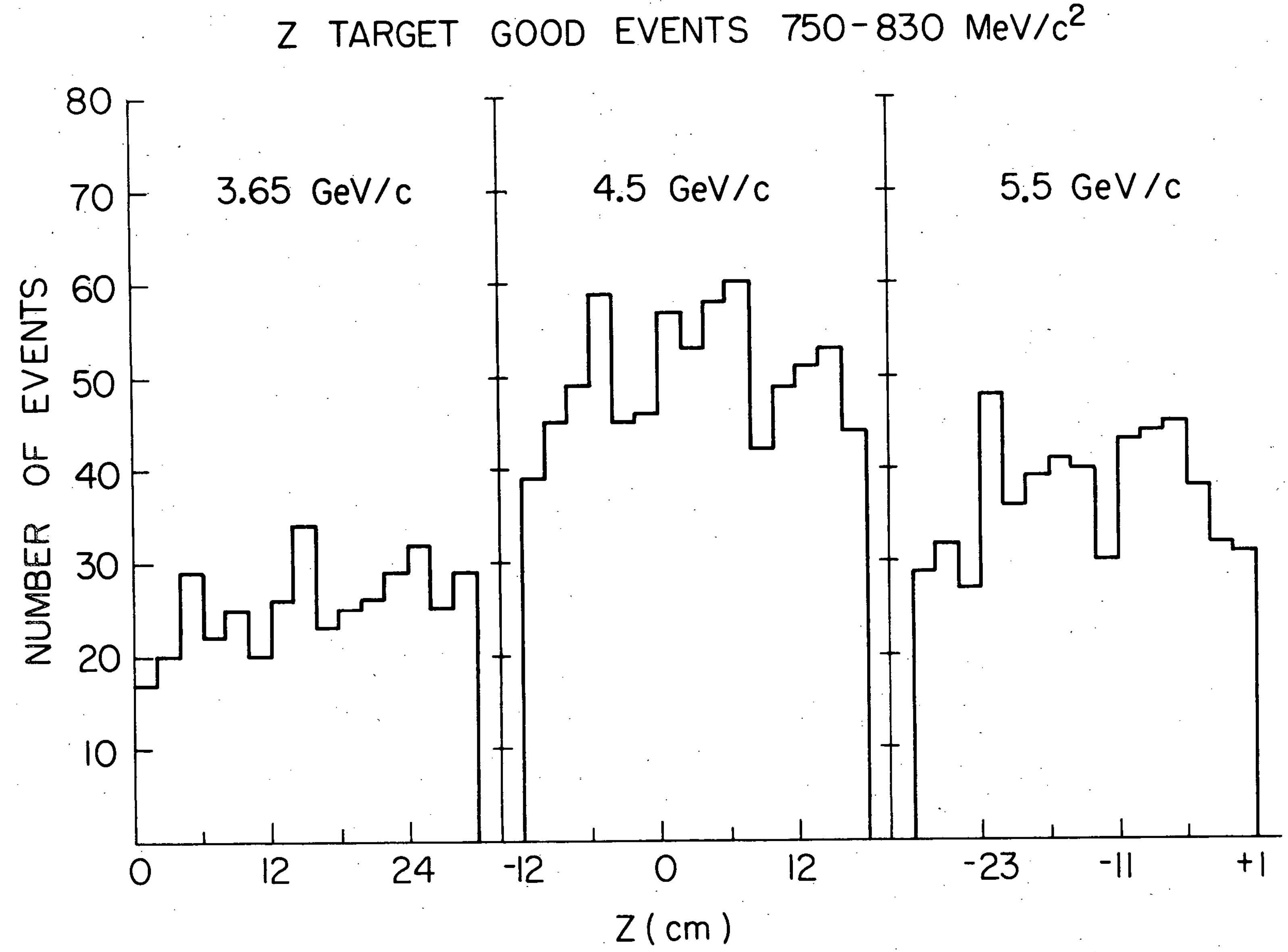
Z TARGET GOOD EVENTS 750-830 MeV/c^2
NUMBER OF EVENTS
80
70
60
50
40
30
20
10
3.65 GeV/c
4.5 GeV/c
5.5 GeV/c
0
12
24
-12
0
12
-23
-11
+1
Z (cm)

V. RESULTS AND CONCLUSIONS

The density matrix elements ρ_{oo}, ρ_{1-1} and $\mathrm{Re}\rho_{10}$ are calculated in the Gottfried-Jackson frame. This coordinate system is defined with the z axis along the incident pion direction as seen in the ω^o rest frame, the y axis along the normal to the production plane, i.e., $\hat{y} = \vec{p}_B \times \vec{p}_\omega$ in the lab, and $\hat{x} = \hat{y} \times \hat{z}$. The density matrix elements are evaluated as moments of the angular distribution, equation II.3, weighted by equation IV.2. Thus

$$\rho_{oo} = \langle \frac{5}{2} \cos^2\theta - \frac{1}{2} \rangle \tag{V.1}$$

$$\rho_{1-1} = \langle - \frac{5}{4} \sin^2\theta \cos 2\varphi \rangle \tag{V.2}$$

and

$$\mathrm{Re}\rho_{10} = \langle - \frac{5}{4\sqrt{2}} \sin 2\theta \cos\varphi \rangle \tag{V.3}$$

These equations are applied to both the ω^o region and the two control regions. The final density matrix element is then given by

$$\rho_{ij} = \frac{N^\omega \rho_{ij}^\omega - N^B \rho_{ij}^B}{N^\omega - N^B} \tag{V.4}$$

where N^ω is the total number of events in the ω^o region, N^B is the number of background events in the ω^o region, ρ_{ij}^ω is the density matrix element calculated for the ω^o region, and ρ_{ij}^B is the density matrix element calculated for the control regions. The final results are plotted in figures V-1, V-2, and V-3. The combinations $\rho_{11} + \rho_{1-1}$, $\rho_{11} - \rho_{1-1}$ are also calculated directly from the data. Table V.1 presents all of these results.

Implicit in all of the above is the assumption that the spin density matrix elements are independent of the efficiency of the neutron hodoscope. This assumption will be valid if the neutron counter efficiencies are slowly varying functions of t, i.e., if in all the t-bins an average neutron counter efficiency can be defined. This assumption is consistent with the results of a computer program which calculates neutron counter efficiencies.[21] Only at low $|t|$, $|t| < .15\ (\mathrm{GeV}/c)^2$, do the calculated neutron counter efficiencies differ significantly within the t bin.

None of the predictions of the simple models in Chapter II are in agreement with the data. Both ρ_{oo} and $\rho_{11} + \rho_{1-1}$ are non-zero indicating the presence of both ρ- and B-exchanges. However, the dip predicted for the ρ trajectory does not occur in $\rho_{11} + \rho_{1-1}$.

It is evident that natural parity exchange dominates; $|\rho_{11} + \rho_{1-1}| > |\rho_{11} - \rho_{1-1}|$, and something other than B-exchange is compensating for the ρ, i.e., something other than the B fills in the ρ dip.

We conclude that a more detailed model is necessary to fit these data.

Table V.1

ω^o DENSITY MATRIX ELEMENTS

Incident Energy (GeV/c)		$.05\le\|t\|<.15$	$.15\le\|t\|<.25$	$.25\le\|t\|<.35$	$.35\le\|t\|<.50$	$.50<\|t\|<1.0$
3.65						
	ρ_{oo}	.58±.11	.27±.08	.27±.09	.19±.08	.50±.11
	ρ_{1-1}	.29±.10	.05±.08	.20±.09	.07±.09	.05±.07
	$\mathrm{Re}\rho_{10}$	.06±.05	-.02±.05	-.04±.04	-.05±.04	.17±.04
	$\rho_{11}+\rho_{1-1}$	.41±.12	.38±.09	.59±.11	.48±.10	.32±.10
	$\rho_{11}-\rho_{1-1}$	.07±.02	.34±.05	.20±.06	.33±.06	.22±.05
4.5						
	ρ_{oo}	.30±.08	.36±.06	.19±.06	.19±.06	.30±.08
	ρ_{1-1}	.24±.06	.23±.05	.17±.06	.20±.06	.26±.06
	$\mathrm{Re}\rho_{10}$	-.06±.03	-.01±.03	.04±.03	-.02±.03	.04±.03
	$\rho_{11}+\rho_{1-1}$	.58±.08	.55±.07	.55±.07	.62±.07	.57±.09
	$\rho_{11}-\rho_{1-1}$	.21+.04	.12±.04	.30±.04	.21±.04	.20±.03
5.5						
	ρ_{oo}	.38±.08	.36±.07	.09±.07	.13±.09	.48±.11
	ρ_{1-1}	.34±.06	.24±.05	.22±.07	.27±.07	.26±.08
	$\mathrm{Re}\rho_{10}$	-.02±.03	-.05±.03	-.05±.03	-.01±.04	.10±.04
	$\rho_{11}+\rho_{1-1}$	.66±.08	.54±.08	.68±.07	.64±.07	.47±.10
	$\rho_{11}-\rho_{1-1}$	.07±.04	.13±.04	.26±.05	.31±.06	.08±.04

Figure V-1 Results for ρ_{oo}.

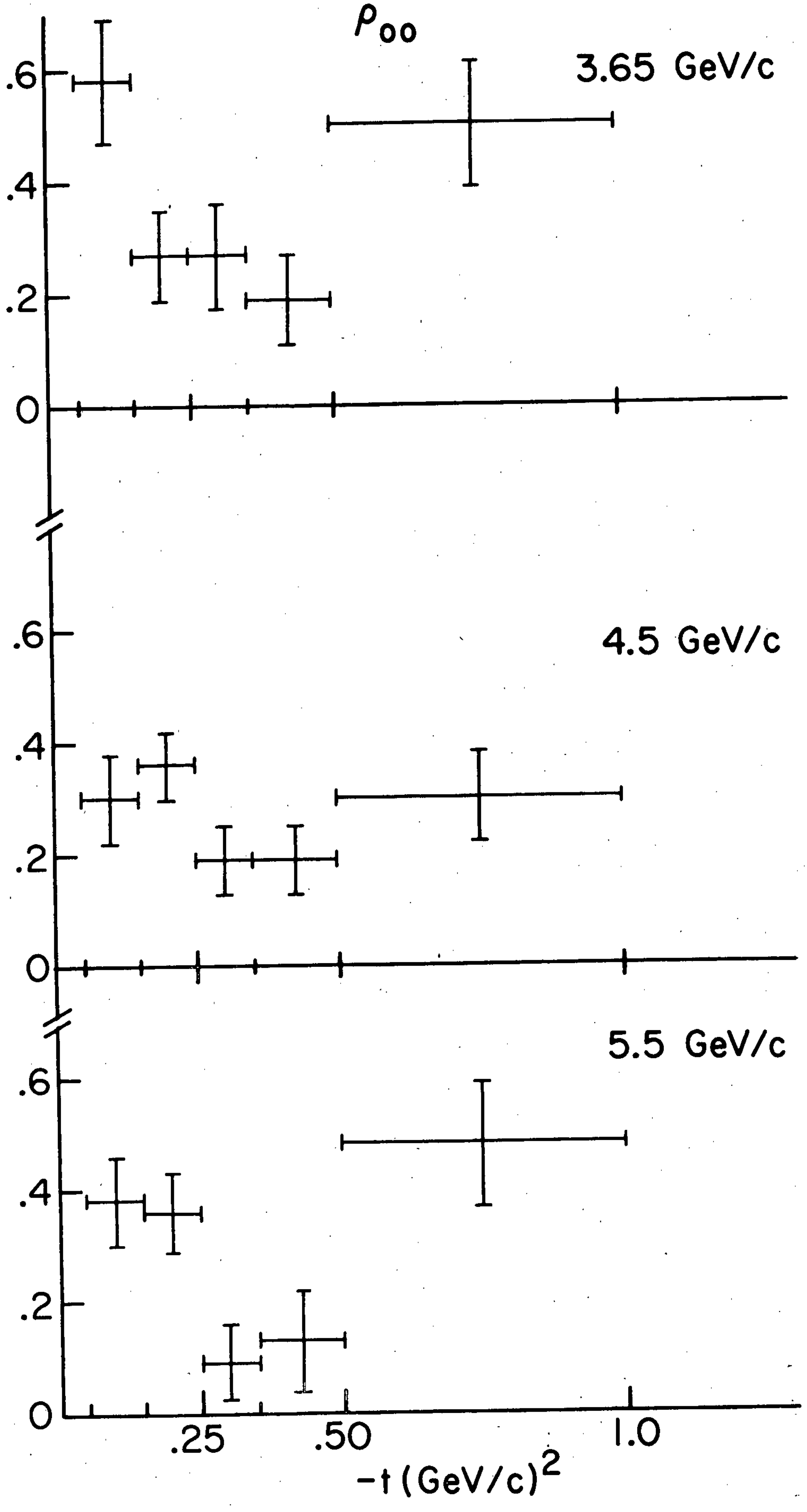
ρ_{00}
3.65 GeV/c
4.5 GeV/c
5.5 GeV/c
.6
.4
.2
0
.25
.50
1.0
-t (GeV/c)^2

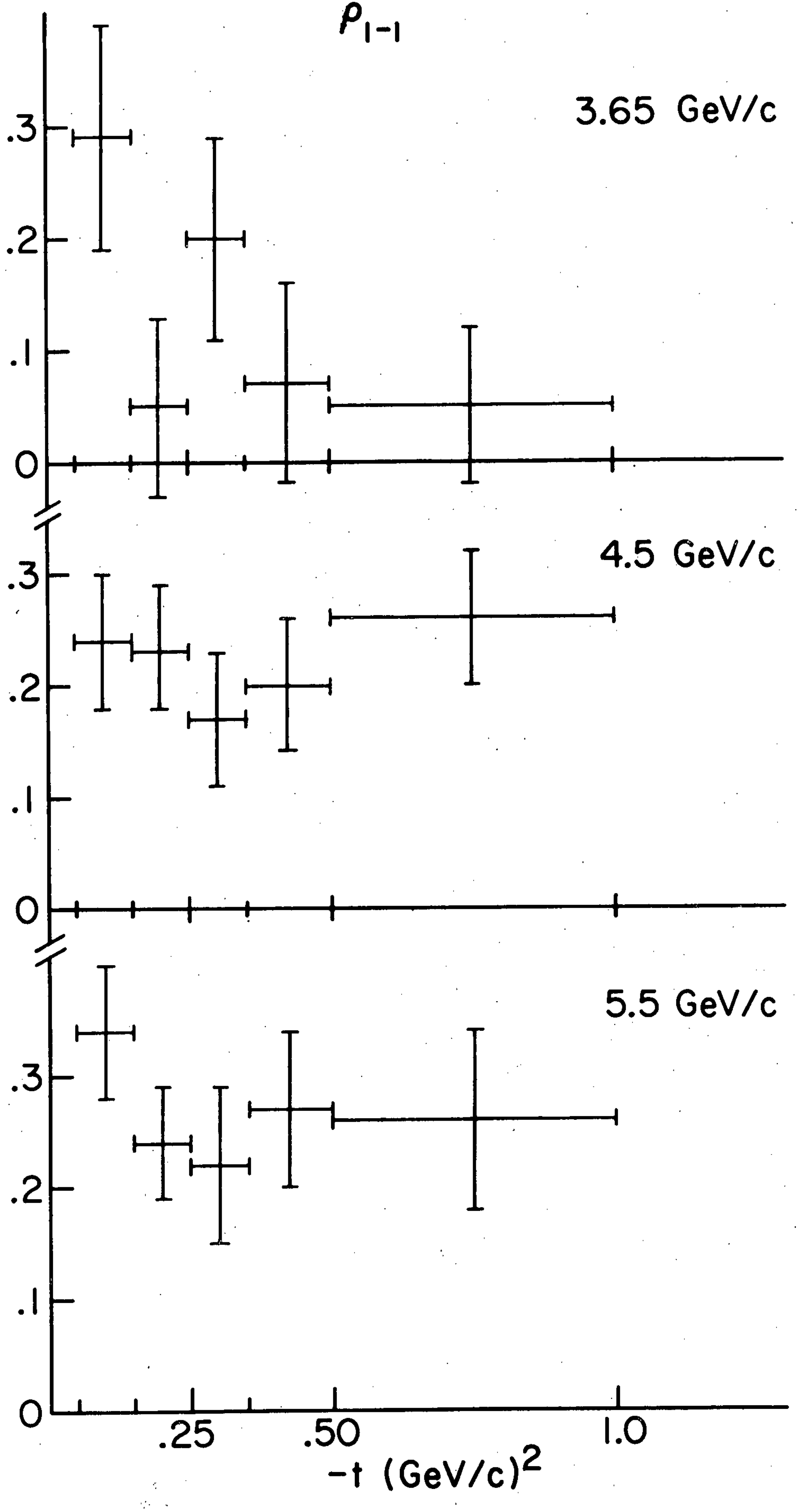
ρ_{1-1}
3.65 GeV/c
4.5 GeV/c
5.5 GeV/c
.3
.2
.1
0
.25
.50
1.0
$-t\ (\mathrm{GeV/c})^2$

Figure V-3 Results for Rep$_{10}$.

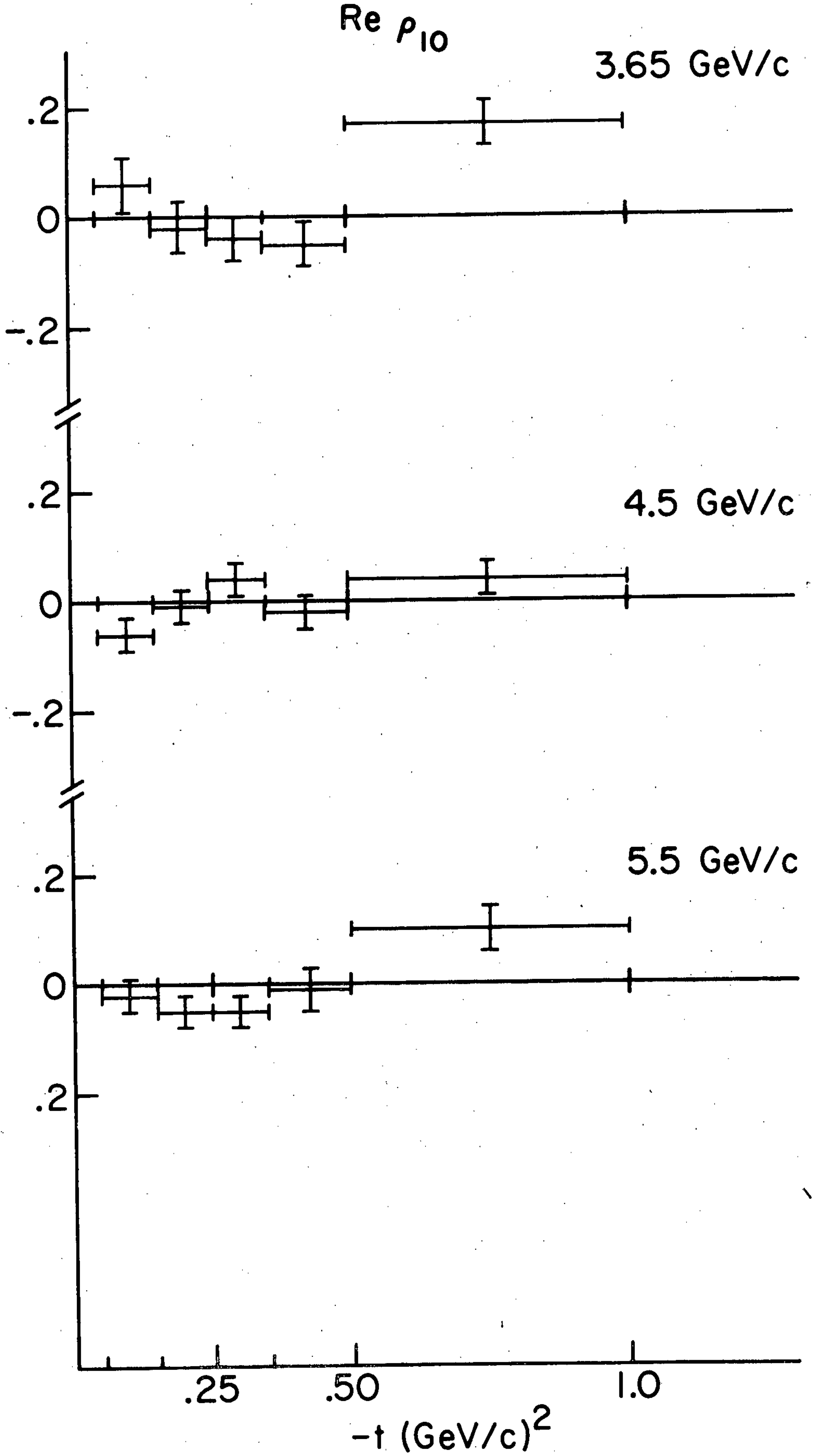
Re ρ10
3.65 GeV/c
4.5 GeV/c
5.5 GeV/c
.2
0
-.2
.2
0
-.2
.2
0
.2
.25
.50
1.0
−t (GeV/c)²

APPENDIX

A. Notation, Conventions and Definitions

We consider the two body reaction AB→CD in the s-channel. The corresponding t-channel reaction is $\bar{D}B \rightarrow C\bar{A}$. (Figure A-1)

The same letter will be used to denote a particle and its helicity, and all quantities will be evaluated in the center of momentum (cm) frame of the channel. Momenta will be denoted by a p plus a particle subscript in the s-channel, and by a q plus a particle subscript in the t-channel.

The Mandelstam variables s, t, u are given by

$$s = (p_A + p_B)^2 = (q_{\bar{A}} - q_B)^2 \qquad \text{(A.1a)}$$

$$t = (p_C - p_A)^2 = (q_C + q_{\bar{A}})^2 \qquad \text{(A.1b)}$$

$$u = (p_D - p_A)^2 = (q_{\bar{A}} - q_{\bar{D}})^2 \qquad \text{(A.1c)}$$

where $a \cdot b = a_o b_o - \vec{a} \cdot \vec{b}$.

The s-channel cm 3-momenta are given by

$$p = |\vec{p}| = |\vec{p}_{AB}| = \frac{\lambda(s, m_A^2, m_B^2)}{2\sqrt{s}} \qquad \text{(A.2a)}$$

and

$$p' = |\vec{p}\,'| = |\vec{p}\,'_{CD}| = \frac{\lambda(s, m_C^2, m_D^2)}{2\sqrt{s}} \qquad \text{(A.2b)}$$

where

$$\lambda(x,y,z) = x^2+y^2+z^2-2xy-2xz-2yz$$

The corresponding t-channel cm 3-momenta are

Figure A-1. Particle Labelling for s- and t- channels.

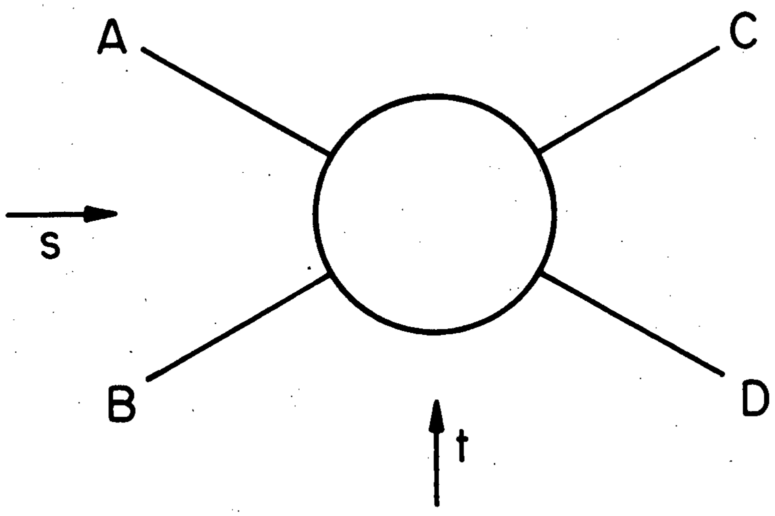

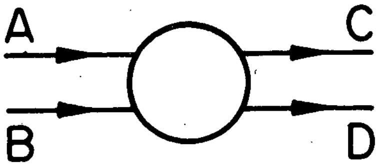

s-CHANNEL

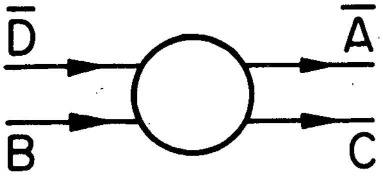

t-CHANNEL

$$q = |\vec{q}| = |\vec{q}_{\bar{D}B}| = \frac{\lambda(t,m_D{}^2,m_B{}^2)}{2\sqrt{t}} \tag{A.3a}$$

and

$$q' = |\vec{q}\,'| = |\vec{q}\,'_{C\bar{A}}| = \frac{\lambda(t,m_C{}^2,m_A{}^2)}{2\sqrt{t}} \tag{A.3b}$$

The s-channel cm scattering angle is given by

$$\cos\theta_s = \frac{s(t-u)-(m_A{}^2-m_B{}^2)(m_C{}^2-m_D{}^2)}{\lambda(s,m_A{}^2,m_B{}^2)\lambda(s,m_C{}^2,m_C{}^2)} \tag{A.4a}$$

and the t-channel cm scattering angle is given by

$$\cos\theta_t = \frac{t(s-u)-(m_A{}^2-m_C{}^2)(m_B{}^2-m_D{}^2)}{\lambda(t,m_A{}^2,m_C{}^2)\lambda(t,m_B{}^2,m_D{}^2)} \tag{A.4b}$$

We use the helicity formalism of Jacob and Wick[22] to describe the s-channel process AB→CD. The z axis is taken along the direction of particle A and the y axis is along the normal to the production plane. In terms of d-functions, the helicity matrix elements describing the reaction become

$$\langle \theta_s 0CD|S|00AB\rangle = \frac{1}{4\pi}\sum_J (2J+1)\langle CD|S^J|AB\rangle d^J_{\lambda\mu}(\theta_s) \tag{A.5}$$

where $\lambda = A-B$, $\mu = C-D$.

Note we have set $\varphi=0$, i.e., the scattering takes place in the x-z plane.

The relation between the invariant Feynman amplitude g and the S matrix is

$$S_{ij} = \delta_{ij} - i(2\pi)^4 (p_i - p_j) \frac{g_{ij}}{\sqrt{\pi_i 2E_i \pi_j 2E_j}} \tag{A.6}$$

and the relationship between our g_{ij} and that of Jacob and Wick is

$$g_{ij} = -8\pi \left(\frac{sp}{p'}\right)^{1/2} g_{ij}^{J\text{-}W}$$

We define

$$g_{CD;AB} = \sum_J (2J+1)\, G^J_{CD;AB}\, d^J_{\lambda\mu}(\theta_s) \tag{A.7}$$

where $G^J_{CD;AB} = \frac{1}{4\pi} \langle JM\, CD | g | JMAB \rangle$ is the partial wave helicity matrix element between the initial and final states. The differential cross section in terms of g is

$$\frac{d\sigma}{d\Omega} = \frac{p'}{64\pi^2 sp} \frac{\sum_{ABCD} |g_{CD;AB}|^2}{(2s_A+1)(2s_B+1)} \tag{A.8}$$

where s_A and s_B are the spins of particles A and B.

Parity acting on a Jacob-Wick state $|JM\lambda_i\lambda_j\rangle$ gives

$$p|JM;\lambda_i\lambda_j\rangle = \eta_i\eta_j(-1)^{J-S_i-S_j}|JM;-\lambda_i-\lambda_j\rangle \tag{A.9}$$

where η_i, η_j and S_i, S_j are the intrinsic parities and spins of particles i and j. Parity acting on the matrix elements G gives

$$G^J_{CD;AB} = \eta' \, G^J_{-C-D;-A-B} \tag{A.10}$$

where $\eta' = \frac{\eta_A \eta_B}{\eta_C \eta_D}(-1)^{S_A+S_B-S_C-S_C}$ and where we have assumed parity conservation in the strong interactions. From the properties of the d-functions, we find

$$g_{CD;AB} = (-1)^{\lambda-\mu} \eta' g_{-C-D;-A-B} \tag{A.11}$$

Using A.9, states of definite parity, $P = \eta(-1)^{J-\epsilon}$ (ϵ=0 for integral J, ϵ=1/2 for half-integral J, $\eta = \pm 1$), can be defined.

$$p|JM\lambda_i\lambda_j\rangle_\eta = \frac{1}{\sqrt{2}}\{|JM;\lambda_i\lambda_j\rangle + \eta\eta_i\eta_j(-1)^{S_i+S_j-\epsilon}|JM;-\lambda_i\lambda_j\rangle\} \tag{A.12}$$

The matrix element connecting two states of definite parity is found using A.11 and A.12.

$$G^{J\eta}_{CD;AB} = G^J_{CD;AB} + \eta\eta_C\eta_D(-1)^{S_C+S_D-\epsilon} \, G^J_{-C-D;AB} \tag{A.13}$$

Equations A.7-A.13 hold for the corresponding t-channel quantities. For clarity we use f and F for t-channel amplitudes and g and G for the s-channel amplitudes as above.

Finally we list some properties of the d-functions.[22]

$$d^J_{mm'}(\theta) = (-1)^{m-m'} d^J_{m'm}(\theta) = d^J_{-m',-m}(\theta) = d^J_{m'm}(-\theta)$$

$$= (-1)^{J-m} d^J_{m-m'}(\pi-\theta) = (-1)^{J+m'} d^J_{m-m'}(\pi+\theta) \qquad (A.14)$$

B. The $\omega^o \to \pi^+\pi^-\pi^o$ Decay Angular Distribution

The use of the decay angular distribution of the three body decay of a resonance to determine the possible spin-parity assignments for the resonance has been described by Berman and Jacob.[23] Their approach is quite general, and if the spin-parity of the resonance is known, the angular distribution in terms of the density matrix elements can be found.[24] Rather than take this general approach, we use our knowledge of the decay amplitude to generate the decay angular distribution.

The matrix element for $\omega^o \to \pi^+\pi^-\pi^o$ is[4]

$$\vec{\epsilon}\cdot\hat{n} \qquad (B.1)$$

in the ω^o rest frame. $\vec{\epsilon}$ is the ω^o polarization vector, and $\hat{n}$ is the unit normal to the decay plane. (We have ignored the dependence on the Dalitz plots variables, i.e., on the pion 3-momenta). In a right-handed coordinate system

$$\hat{n} = (\sin\theta\cos\varphi,\ \sin\theta\sin\varphi,\ \cos\theta) \qquad (B.2)$$

and in terms of spin components for a pure ω^o state α

$$\vec{\epsilon} = C_1^\alpha \epsilon_+ + C_{-1}^\alpha \epsilon_- + C_o^\alpha \epsilon_o \qquad \text{(B.3)}$$

where C_1^α is the probability amplitude that the ω^o has z-component of spin = i, and $\epsilon_\pm = \mp \frac{1}{\sqrt{2}}(1,\pm i,0)$, $\epsilon_o = (0,0,1)$. Thus

$$\vec{\epsilon}\cdot\hat{n} = -\frac{C_1^\alpha}{\sqrt{2}}\sin\theta\; e^{i\varphi} + \frac{C_{-1}^\alpha}{\sqrt{2}}\sin\theta\; e^{-i\varphi} + C_0^\alpha\cos\theta \qquad \text{(B.4)}$$

The angular distribution is proportional to $\Sigma\, p^\alpha|\vec{\epsilon}\cdot\hat{n}|^2$. The ω^o spin-density matrix elements, $\rho_{ij} = \sum_\alpha C_i^\alpha C_j^\alpha p^\alpha$ where p^α is the probability of being in pure state α ,

We now find

$$\begin{aligned} w(\theta,\varphi) \sim\; & \rho_{11}\frac{\sin^2\theta}{2} + \rho_{-1-1}\frac{\sin^2\theta}{2} + \rho_{00}\cos^2\theta - \rho_{1-1}\frac{\sin^2\theta}{2}\, e^{-2i\varphi} \\ & -\rho_{10}\frac{\sin\theta\cos\theta}{\sqrt{2}}\, e^{-i\varphi} - \rho_{-11}\frac{\sin^2\theta}{2}\, e^{2i\varphi} + \rho_{-10}\frac{\sin\theta\cos\theta}{\sqrt{2}}\, e^{i\varphi} \\ & -\rho_{01}\frac{\sin\theta\cos\theta}{\sqrt{2}}\, e^{i\varphi} + \rho_{0-1}\frac{\sin\theta\cos\theta}{\sqrt{2}}\, e^{-i\varphi} \qquad \text{(B.5)} \end{aligned}$$

If the z axis, i.e., the spin quantization axis, lies in the ω^o production plane (see Appendix C), then $\rho_{mm'} = (-1)^{m-m'}\rho_{-m-m'}$.

Also the density matrix is Hermitian so

$$\rho_{mm'} = \rho^*_{m'm}$$

Using these two relations

$$w(\theta,\varphi) \sim \rho_{11}\sin^2\theta + \rho_{00}\cos^2\theta - \rho_{1-1}\sin^2\theta\cos 2\varphi - 2\sqrt{2}\ \mathrm{Re}\rho_{10}\sin\theta\cos\theta\cos\varphi$$

where $\rho_{11} = \frac{1-\rho_{oo}}{2}$ by the unit trace requirement, and ρ_{1-1} is real. Normalizing $w(\theta,\varphi)$ we finally find

$$w(\theta,\varphi) = \frac{3}{4\pi}[\rho_{11}\sin^2\theta+\rho_{00}\cos^2\theta-\rho_{1-1}\sin^2\theta\cos 2\varphi-\sqrt{2}\ \mathrm{Re}\ \rho_{10}\ \sin 2\theta\cos\varphi] \qquad (B.7)$$

C. Properties of the Spin 1 Density Matrix

As in the main text, and Appendix A we consider the two body reaction AB→CD. In terms of the t-channel helicity amplitudes

$$\rho_{\lambda\lambda'} = \sum_{ABC} f_{c\lambda;AB} f^*_{C\lambda';AB} \qquad (C.1)$$

in the Gottfried-Jackson frame.[8]

From A.11,

$$\begin{aligned}
\rho_{\lambda\lambda'} &= \sum_{ABC} (-1)^{A-B-(C-\lambda)} f_{-C-\lambda;-A-B} (-1)^{(\lambda'-C)-(A-B)} f_{-C-\lambda';-A-B} \\
&= (-1)^{\lambda-\lambda'} \sum_{ABC} f_{-C-\lambda;-A-B} f^*_{-C-\lambda';-A-B} \\
&= (-1)^{\lambda-\lambda'} \sum_{ABC} f_{C-\lambda' AB} f^*_{C-\lambda';AB} \\
&= (-1)^{\lambda-\lambda'} \rho_{-\lambda-\lambda'} \qquad (C.2)
\end{aligned}$$

The only restriction in deriving C.2 is that the scattering takes place in the x-z plane. The Jackson-Gottfried frame satisfies this condition. For a spin one object, we find

$$\rho_{11} = \rho_{-1-1};$$

$$\rho_{10} = -\rho_{-10}; \rho_{1-1} = \rho_{-11}.$$

Since the spin-density matrix is Hermitian and has unit trace

$$\rho_{00} = 1-\rho_{11}-\rho_{-1-1} = 1-2\rho_{11}$$

$$\rho_{10} = \rho_{01}^{*} = -\rho_{0-1}^{*}$$

$$\rho_{1-1} = \rho_{-11}^{*} = \rho_{1-1}^{*} \qquad \text{is real}$$

Thus

$$\tilde{\rho} = \begin{pmatrix} \rho_{11} & \rho_{10} & \rho_{1-1} \\ \rho_{10}^{*} & \rho_{00} & -\rho_{10} \\ \rho_{1-1} & -\rho_{10}^{*} & \rho_{11} \end{pmatrix}$$

where $\rho_{00} = 1-2\rho_{11}$, and ρ_{11}, ρ_{1-1} are real.

LIST OF REFERENCES

1. B. C. Maglic, L. W. Alvarez, A. M. Rosenfeld, and M. L. Stevenson, Phys. Rev. Letters 7, 178 (1961).
2. S. M. Flatte, D. O. Huwe, J. J. Murray, J. Button-Shafer, F. T. Solmnitz, M. L. Stevenson, and C. Wohl, Phys. Rev. 145, 1050 (1966).
3. Particle Data Group, Phys. Letters 33B, 1 (1970).
4. C. Zemach, Phys. Rev. 133, B1201 (1964).
5. R. H. Dalitz, Strong Interactions, Ed. L. W. Alvarez (Academic Press, New York, 1965) p. 141.
6. P. Minneart, Phys. Rev. Letters 16, 672 (1966).
7. R. J. Eden, High Energy Collision of Particles (Cambridge University Press, London, 1967) p. 122.
8. K. Gottfried and J. D. Jackson, Nuovo Cimento 33, 309 (1964).
9. L. Jones, Phys. Rev. 163, 1523 (1967).
10. J. D. Jackson and G. E. Hite, Phys. Rev. 169, 1248 (1968).
11. M. Gell-Mann, M. L. Goldberger, F. E. Low, E. Marx, and F. Zachariasen, Phys. Rev. 133, B145 (1964).
12. L. L. Wang, Phys. Rev. 153, B145 (1964).
13. J. P. Ader, M. Capdeville, G. Cohen-Tannoudji, and Ph. Salin, Nuovo Cimento 51A, 952 (1965).
14. L. L. Wang, Phys. Rev. Letters 16, 756 (1966).
15. M. Barmawi, Phys. Rev. 166, 1857 (1968).
16. M. Nobuyama, Progr. Theoret. Phys. (Kyoto) 41, 730 (1969).
17. N. N. Achasov and G. N. Shestakov, Reported at the XV International Conference on High Energy Physics, (Kiev, 1970).
18. G. S. Abrams and U. Maor, Phys. Rev. Letters 25, 621 (1970).
19. A. D. Russell, Ph.D. Thesis, University of Illinois (Expected 1971).

20. R. W. Downing, D. W. Mortara, and C. A. Schaad, "The Scanning and Measuring Projector", University of Illinois, 1966 (Physics Department Internal Report).

21. R. J. Kurz, UCRL-11339, 1964 (Unpublished).

22. M. Jacob and G. C. Wick, Ann. Phys. (N.Y.) 7, 404 (1959).

23. S. M. Berman and M. Jacob, Phys. Rev. 139, B1023 (1965).

24. J. D. Jackson, High Energy Physics, Ed. C. Dewit and M. Jacob, (Gordon and Breach, New York, 1965), p. 326.

25. G. C. Benson, B. P. Roe, D. Sinclair, and J. C. VanderVelde, Phys. Rev. Letters 22, 1074 (1969).

26. B. Eisenstein and H. Gordon, Phys. Rev. Letters 23, 673 (1969).

27. J. A. J. Matthews, J. D. Prentice, T. S. Youn, J. T. Carroll, M. V. Firebaugh and W. D. Walker, Phys. Rev. Letters 26, 400 (1971).

VITA

Eli Ira Rosenberg was born in [redacted] He attended public schools in Brooklyn and graduated from Samuel J. Tilden High School in June, 1960. He entered the City College of New York in September, 1960, and received the Bachelor of Science degree, cum laude, in June, 1964.

He has attended the Graduate College at the University of Illinois continuously since February, 1965, holding a combination of research and teaching assistantships. He is co-author of the paper "A Measurement of the Ratio of the τ' Partial Decay Rates: $\Gamma(K^- \to \pi^- \pi^o \pi^o)/\Gamma(K^+ \to \pi^+ \pi^o \pi^o)$," Phys. Rev. 186, 1403 (1969).

He is a member of Phi Beta Kappa, the American Physical Society, and the American Association for the Advancement of Science.